Results in Engineering 27 (2025) 106027

Contents lists available at ScienceDirect

Results in Engineering

journal homepage: www.sciencedirect.com/journal/results-in-engineering

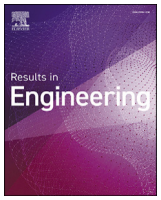

Research paper

Assessing thermal and hydrodynamic performance of non-Newtonian nano-coolant flow through a porous backward-facing step channel with non-Darcian effects

Zarin Akter [a,b], Preetom Nag [a,b,*], Hasina Akter [a,b], Md. Mamun Molla [a,b], Goutam Saha [c]

[a] Department of Mathematics & Physics, North South University (NSU), Dhaka-1229, Bangladesh
[b] Center of Applied & Computational Sciences (CACS), NSU, Dhaka-1229, Bangladesh
[c] Department of Mathematics, University of Dhaka, Dhaka-1000, Bangladesh

ARTICLE INFO

Keywords:
Non-Newtonian fluid
Nanofluid
Porous medium
Backward facing step
Finite volume method
Performance evaluation criteria

ABSTRACT

This research examines the hydrodynamic and thermal characteristics of Al_2O_3-water as a shear-thinning non-Newtonian nano-coolant (NC) flowing through a porous structure. The rheological characteristics of the coolant have been deemed to be shear-thinning based on the weight percentage (ϕ) of suspended nanoparticles. The flow dynamics are examined within a homogeneous saturated porous substrate placed in a backward-facing step (BFS) channel featuring an expansion ratio of 1:2. The lengths of the upstream and downstream channels, before and after the step of height h, are maintained in a ratio of $6h : 30h$. The Darcy–Brinkman–Forchheimer (DBF) porous model, incorporating non-Newtonian viscous NC flow, has been numerically solved within the computational domain using a finite volume method with second-order accuracy. The investigations were conducted with varying key parameters, including Reynolds number ($300 \leq Re \leq 1000$), Rayleigh number ($10^5 \leq Ra \leq 10^6$), porosity ($0.4 \leq \epsilon \leq 0.99$), and Darcy number ($10^{-1} \leq Da \leq 10^{-3}$). Findings indicate a 50% reduction in skin friction coefficient (C_f) when doubling Re, highlighting the complex relationship between flow dynamics and thermal exchange within the porous substrate. The recirculation zone after the step shrinks with decreasing ϵ, emphasizing the improved heat transfer (HT) from the wall interface through a stronger porous medium. Increasing the porous strength by reducing ϵ from 0.9 to 0.4 leads to over 200% improvement in average thermal exchange rate (Nu_{avg}) for the shear-thinning coolant ($\phi = 4\%$) even at low permeability ($Da = 0.001$). The study also evaluates the thermal performance criterion (PEC), which increases with higher Re but decreases with ϕ. The outcomes of PEC provide practical insights into the thermal engineering aspects, underscoring the significance of comprehending nano-coolant dynamics within a porous matrix for optimizing thermal transport processes.

1. Introduction

The pursuit of high-performance thermal systems has become a cornerstone of innovation across various fields of science and engineering. Managing thermal systems in electronic cooling and optimizing the heat transfer (HT) rate is crucial for thermal engineering systems [1]. A promising approach for enhancing the HT phenomena lies in using fluid-saturated porous media, which shows diverse thermal engineering applications, including hydrology, civil and mechanical engineering, and chemical and petroleum engineering [2]. To utilize porous media effectively, it is essential to model the coupled momentum and energy transfer phenomena with sufficient accuracy. Over the past decades, both experimental and theoretical research have explored transport behavior in homogeneous, saturated porous media. Several momentum models have been developed to represent flow through such media, including Darcy's law for slow flows, and its extended forms: the Brinkman, Forchheimer, and Darcy–Brinkman–Forchheimer (DBF) models. These frameworks help capture the complex interactions between flow resistance and thermal transport [3]. Unlike the classical Darcy or Darcy–Forchheimer models, the DBF model accommodates no-slip boundary conditions and resolves nonlinear momentum losses, which are critical when analyzing confined geometries such as backward-facing step (BFS)

* Corresponding author at: Department of Mathematics & Physics, North South University (NSU), Dhaka-1229, Bangladesh.
E-mail address: preetom.nag@northsouth.edu (P. Nag).

https://doi.org/10.1016/j.rineng.2025.106027
Received 23 March 2025; Received in revised form 23 May 2025; Accepted 29 June 2025
Available online 7 July 2025
2590-1230/© 2025 The Author(s). Published by Elsevier B.V. This is an open access article under the CC BY-NC license (http://creativecommons.org/licenses/by-nc/4.0/).

Nomenclature

English symbols

C_p	Specific heat at constant pressure	($J\,kg^{-1}\,K^{-1}$)
Da	Darcy number	
Ra	Rayleigh number	
Re	Reynolds number	
Ri	Richardson number	
Pe	Peclet number	
S	Local Entropy Generation	
g	Acceleration due to gravity	($m\,s^{-2}$)
Gr	Grashof number	
h	Heat Transfer coefficient	($W\,m^{-2}\,K^{-1}$)
H	Channel height	
k	Thermal conductivity	($w\,m^{-1}\,K^{-1}$)
K	Permeability	
Nu	Nusselt number	
$\bar{p}$	Pressure	(pa)
Pr	Prandtl number	
$\bar{t}$	Time	(s)
T	Temperature of the fluid	(K)
$\bar{u}, \bar{v}$	Dimensional velocity along the horizontal and vertical directions	($m\,s^{-1}$)
$\bar{x}, \bar{y}$	Horizontal and vertical coordinate	($m\,s^{-1}$)

Greek symbols

α	Thermal diffusivity of the base fluid	($m^2\,s^{-1}$)
β	Thermal expansion coefficient	(K^{-1})
$\dot{\gamma}$	Dimensional shear rate	(s^{-1})
η	Non-dimensional shear rate	
θ	Non-dimensional temperature of the fluid	
ϕ	Nanoparticle volume fraction	
μ_f	Dynamic viscosity of the base fluid	($kg\,m^{-1}\,s^{-1}$)
ν_f	Kinematic viscosity of the base fluid	($m^2\,s^{-1}$)
ρ	Density of fluid	($kg\,m^{-3}$)

Subscripts

f	base fluid
nf	nanofluid
avg	average
ff	fluid friction

Acronym

NFs	Nanofluids
HNF	Hybrid Nanofluid
HT	Heat Transfer
NC	Nano-coolant
BFS	Backward-facing step
$EGEN$	Entropy Generation
PEC	Performance Evaluation Criteria

channels [4]. The inclusion of inertial and viscous effects enhances the physical realism of the model, especially under non-Darcian conditions where both flow resistance and recirculation regions strongly influence thermal transport [5]. The effectiveness of this approach has been validated in previous works involving forced and natural convection in porous systems [6].

Despite the considerable attention given to porous media as an effective HT promoter in various industrial applications, another promising avenue for enhancing HT in the thermal engineering industry is the utilization of nanofluids (NFs) for their excellent HT enhancement quality to optimize energy devices [7]. Nanofluids, defined as suspensions of nanoparticles ranging from 1 to 100 nm in size, were first introduced by Choi and represent a novel class of nanotechnology-based HT fluids [8]. These fluids are often created by mixing nanoparticles into conventional liquids such as water, oil, and ethylene glycol [9]. The improved performance of nanofluid HT compared to the traditional fluids arises from the enhanced thermal conductivity and improved energy exchange capability resulting from the suspended ultrafine particles. Both experimental and numerical studies have indicated that NFs containing Al_2O_3 or CuO nanoparticles can significantly improve thermal conductivity, leading to energy savings of electronic devices and facilitating device miniaturization [10]. Mishra et al. [11] numerically studied HNF flow over a stretching/shrinking sheet, finding that volume fraction, thermal slip, and magnetic effects significantly influence velocity, temperature, and HT performance. Cu–water nanofluid convection in a vertically oriented annulus with non-uniform bottom heating revealed bi-cellular flow structures and improved HT performance with increasing Rayleigh number and nanoparticle concentration [12]. A seminal study by Abu-Nada et al. [13] highlighted the potential of NFs to improve the efficiency of heat exchangers, creating new opportunities to understand their interactions with fluid dynamics and optimize HT mechanisms. The utilisation of NFs to improve HT in boundary layer flow systems has recently attracted significant attention, as it offers a standard setup for research in fluid mechanics on separated flows, addresses various industrial concerns, and has captivated the interest of numerous researchers. Pop et al. [14] emphasized the improved thermal properties of NFs achieved through nanoparticle dispersion, enhancing HT efficiency in applications such as cooling systems. Various nanoparticles [15], including copper, silver, oxides (Al_2O_3, TiO_2, CuO), carbides (SiC, TiC), or carbon nanotubes, are used to enhance the thermal properties of the base fluids.

A review of fluid flow HT within porous media, reported by Shenoy [16], reveals non-linear fluid behavior that differs from the characteristics of Newtonian fluid flow. This non-Newtonian behavior in porous media has attracted significant attention due to its implications for HT efficiency in various practical engineering applications, including oil recovery, food processing, and material processing. The widespread occurrence of non-Newtonian rheology in nanofluid behavior in many industrial processes has led to a growing interest in enhancing HT efficiency and flow control in porous media, making them crucial for optimizing thermal systems, industrial processes, and energy applications due to their adaptable rheological properties [17,18]. Various numerical methods, such as boundary element, finite element, finite volume, finite difference, and the smooth particle hydrodynamics (SPH) method, have been used to study non-Newtonian fluid flows and nanofluids (NFs), providing key insights into their rheological behavior and flow characteristics [19–21]. Hojjat et al. [22] reported the non-Newtonian rheology of aqueous solution of Al_2O_3, TiO_2, CuO nanoparticles with various concentrations ($0 \leq \phi \leq 1.5$) and operating temperatures ($5\,°C \leq T \leq 45\,°C$). The rheological behavior has been characterized by the non-Newtonian power-law model with experimentally observed consistency index and power-law index, exhibiting the pseudoplastic or shear-thinning behavior of the mentioned nanofluids, making the fluid suitable for diverse industrial applications such as drilling and pharmaceuticals [23,24]. The influence of power-law behaviors and non-Newtonian consistency indices on flow patterns and heat transmission mechanisms of Al_2O_3 nanofluids was extensively examined by Santra et al. [25] and Nazari et al. [26] in different research. Their work emphasizes the behavior of non-Newtonian fluids in complex geometries, which aids in optimizing the practical applications of HT efficiency. The addition of Al_2O_3 improves HT performance, thereby enhancing efficiency and flow control in porous media [27].

This combined effect of non-Newtonian properties and increased thermal conductivity optimizes thermal systems and energy applications. Khan et al. [28] analyzed MHD Maxwell HNF flow over a porous stretching sheet, showing that multiple slip conditions and thermal radiation significantly impact skin friction, heat, and mass transfer behavior.

Studies of non-Newtonian NFs in step flows that face backward, as reported by various researchers [29,30], offer new understandings of heat transmission and fluid dynamics. It is notable for expressing that fluid separation and reattachment length in the flow of non-Newtonian NFs through a physical system significantly affect HT and flow behavior. The BFS flow exemplifies these dynamics, offering insights for optimizing HT and turbulence modeling [31]. In the field of fluid mechanics, the term "backward-facing step" refers to a sudden expansion in a flow passage commonly encountered in various industrial and engineering applications, such as engine flows, the spoiler flows, separation flow behind an airfoil, vehicle (cars and boats), heat transfer systems, inlet tunnel flow of engine, or inside a condenser/combustor, and even the flow around buildings or architectural complex [32]. This flow configuration is of significant interest for understanding and analyzing complex fluid dynamics, particularly phenomena such as flow separation, vortex evolution, recirculation, and reattachment. These aspects are essential for comprehending flow dynamics in applications like vehicle aerodynamics and heat exchangers. The fundamental physics of BFS flow has garnered considerable attention in recent years, especially under critical conditions, such as during aircraft stalling. Moreover, effective mixing is desirable in certain applications, such as mixing chambers or combustors. By incorporating detailed geometric considerations of BFS, researchers can investigate various mechanisms and control strategies within this domain. Researchers use experiments and numerical simulations to explore flow physics, thermal characteristics, and HT optimization, with studies examining various aspects of BFS flow, including turbulent shear layers, mixed convection, and laminar pulsating flow [33,34]. For instance, earlier a study by Armaly et al. [35] explored experimental and theoretical aspects of BFS flow using air, reporting results for Re numbers ranging from $70 \leq Re \leq 8000$, covering laminar, transitional, and turbulent airflow. The study revealed that the reattachment point moves downstream and away from the step with increasing Re numbers. Another pioneering study on 2D BFS flow through numerical simulations and experimental methods [36] focused on air as a working fluid, considering Re numbers of up to 3000 and expansion ratios of 1.17 and 2.0 in the channel. Additionally, Erturk [37] conducted a comprehensive examination of 2D steady incompressible Navier-Stokes equations for flow over a BFS at high Re numbers, employing an efficient finite difference method to present results graphically and in tabular formats. Swain et al. [38] numerically investigated 3D Maxwell nanofluid flow over a stretching surface, revealing that nanoparticle aggregation enhances thermal conductivity, while magnetic, radiation, and heat source effects shape HT behavior.

To optimize energy efficiency and HT performance in thermal systems, studying entropy generation has become crucial as it reflects thermodynamic irreversibility and associated energy loss. Recent research has delved into unravelling the entropy generation in flows through BFS configurations within porous media using a mix of numerical simulations and experimental investigations. These inquiries yield valuable insights into how geometric configurations, Re number, and Da number influence the rates at which entropy is generated [39]. As fluid traverses through porous media in a BFS geometry, entropy generation arises from the interactions of viscous dissipation, heat transfer, and flow characteristics [40]. Mansour et al. [41] revealed that heat sources in MHD natural convection of Al_2O_3-Cu/water hybrid nanofluids could enhance thermal efficiency by promoting uniform temperature distributions and minimizing entropy generation in porous cavities. By gaining a thorough understanding of entropy generation in BFS flows through porous media, researchers strive to enhance HT efficiency, minimize energy losses, and develop more effective engineering systems [42]. Minimizing entropy generation is crucial for improving thermal performance, as it directly correlates with reducing energy dissipation and enhancing overall HT efficiency, leading to more optimized and efficient thermal designs [43]. Kong et al. [44] comprehensively evaluated Al_2O_3 nanofluid as an enhanced HT fluid. They focused on critical performance criteria such as thermal conductivity, HT rate, and temperature distribution. The study aimed to quantitatively assess the advantages of Al_2O_3 nanofluid compared to conventional fluids, shedding light on its potential to improve thermal management strategies in engineering applications. The performance criteria for heat exchangers primarily aim to strike a balance between efficiency and practicality [45]. These criteria consider factors such as heat duty, initial cost, pumping power, safety, and compact design.

The literature survey indicates that previous studies on heat transfer within porous structures have not examined the behavior of nanofluids with non-Newtonian rheology in conjunction with non-Darcian effects. This study emphasizes the significance of investigating the Darcy-Brinkman-Forchheimer (DBF) solution in the context of non-Newtonian nanofluids, explicitly focusing on the impact of varying nanoparticle volume fractions as they flow through a BFS porous channel. The novelty of this research lies in its analysis of the thermal and hydrodynamic performance of non-Newtonian Al_2O_3-aqua nanofluids, utilizing experimentally determined rheological parameters that vary with nanoparticle concentration. Furthermore, this study explores thermodynamic irreversibility during heat transfer processes by analyzing entropy generation.

The present study explores the use of finite volume numerical methods to simulate momentum and heat transfer phenomena within the BFS domain. It incorporates non-Newtonian rheology and porous effects, providing crucial insights into enhanced heat transfer rates in regions experiencing flow separation. The research advances by assessing flow characteristics and thermal exchange behavior, considering several key parameters, including the Rayleigh number (Ra), Reynolds number (Re), Darcy number (Da), porosity (ϵ), and the weight percentage (ϕ) of nanoparticles. Simulation results demonstrate that higher nanoparticle volume fractions and Reynolds numbers contribute to increased heat transfer rates, while the BFD model effectively captures pressure losses in the porous medium. The present research explores the performance of nanofluid flow concerning HT enhancement by using performance evaluation criteria (PEC), which addresses the pumping power required to improve the HT rate of highly viscous nano-coolants flowing through a porous medium.

The findings from this study address the significant implications for improving heat exchanger efficiency, optimizing aerodynamic designs, and deepening our understanding of the intricate relationships between fluid dynamics and thermal processes within a condenser or combustor [46]. These insights are valuable for various engineering applications, including engine flows, spoiler flows, separation flow behind an airfoil, and heat transfer systems in vehicles such as cars and boats.

2. Formulation of the problem

2.1. Physical model

In the study of fluid dynamics, the BFS channel flow presents a classic scenario of fluid flow in a sudden channel expansion. This 2-D setup, illustrated in Fig. 1, involves a parabolic inflow of Al_2O_3-water non-Newtonian nano-coolant through a channel of height H, with a step of height $h(= H/2)$. The lengths of the upstream and downstream walls are denoted by $x_i = 6h$ and $x_e = 30h$, respectively. The prescribed velocity profile, $\bar{u}(\bar{y}) = 12U\left[3(\bar{y}/H) - 2(\bar{y}/H)^2 - 1\right]$ $(h \leq \bar{y} \leq H)$, ensures a hydrodynamically stable and fully developed flow at the entrance [35,37], with zero streamwise gradients at the outlet. Additionally, a constant temperature T_C is maintained along the upper straight wall, while the upstream section of the BFS, the step wall itself, and the downstream bottom wall are all heated to a consistent temperature T_H, where $T_H > T_C$.

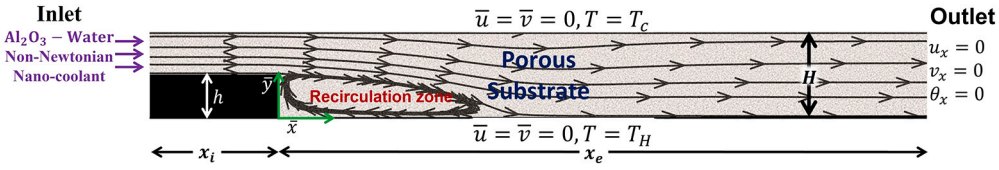

Fig. 1. Schematic of the Backward-facing step with boundary conditions in dimensionless form.

2.2. Flow assumptions

The present study considers the following assumptions to govern the flow in the above-mentioned physical domain,

- A two-dimensional, laminar, incompressible flow with non-Newtonian shear-thinning rheology based on the volume fraction of suspended nanoparticles in the base liquid.
- Dispersed nanoparticles uphold thermal equilibrium so that the no-slip condition is maintained between the host water molecules and the Al_2O_3 nanoparticles [22,47].
- The thermodynamic characteristics of the fluid are constant, except for the density in the buoyancy force term, which is estimated using Boussinesq's approximation.
- The impact of viscous heat dissipation in the fluid is considered negligible compared to the effects of conductive and convective heat transfer.
- The Al_2O_3-water nanofluid maintains weak electrical conductivity at low volume fractions [48,49] of interest, which reduces the significance of induced magnetic effects and Hall currents.

2.3. Governing equations in dimensional form

On the above assumption of the flow, the governing equations within the homogeneous porous medium are formulated based on the non-Darcian model, specifically the Darcy-Brinkman-Forchheimer (DBF) model [50,51].

$$\frac{\partial \bar{u}}{\partial \bar{x}} + \frac{\partial \bar{v}}{\partial \bar{y}} = 0 \tag{1}$$

$$\begin{aligned}&\frac{\rho_{nf}}{\epsilon}\frac{\partial \bar{u}}{\partial \bar{t}} + \frac{\rho_{nf}}{\epsilon^2}\left(\bar{u}\frac{\partial \bar{u}}{\partial \bar{x}} + \bar{v}\frac{\partial \bar{u}}{\partial \bar{y}}\right)\\ &= -\frac{\partial \bar{p}}{\partial \bar{x}} + \frac{1}{\epsilon}\left[\frac{\partial}{\partial \bar{x}}\left(2\mu_{eff}\frac{\partial \bar{u}}{\partial \bar{x}}\right) + \frac{\partial}{\partial \bar{y}}\left(\mu_{eff}\frac{\partial \bar{u}}{\partial \bar{y}} + \mu_{eff}\frac{\partial \bar{v}}{\partial \bar{x}}\right)\right]\\ &\quad - \left(\frac{F_C \cdot \rho_{nf}}{\sqrt{K}}\sqrt{\bar{u}^2 + \bar{v}^2} + \frac{\mu_{eff}}{K}\right)\bar{u}\end{aligned} \tag{2}$$

$$\begin{aligned}&\frac{\rho_{nf}}{\epsilon}\frac{\partial \bar{v}}{\partial \bar{t}} + \frac{\rho_{nf}}{\epsilon^2}\left(\bar{u}\frac{\partial \bar{v}}{\partial \bar{x}} + \bar{v}\frac{\partial \bar{v}}{\partial \bar{y}}\right)\\ &= -\frac{\partial \bar{p}}{\partial \bar{y}} + \frac{1}{\epsilon}\left[\frac{\partial}{\partial \bar{x}}\left(\mu_{eff}\frac{\partial \bar{v}}{\partial \bar{x}} + \mu_{eff}\frac{\partial \bar{u}}{\partial \bar{y}}\right) + \frac{\partial}{\partial \bar{y}}\left(2\mu_{eff}\frac{\partial \bar{v}}{\partial \bar{y}}\right)\right]\\ &\quad - \left(\frac{F_C \cdot \rho_{nf}}{\sqrt{K}}\sqrt{\bar{u}^2 + \bar{v}^2} + \frac{\mu_{eff}}{K}\right)\bar{v} + g\left(\rho\beta_T\right)_{nf}\left(T - T_c\right)\end{aligned} \tag{3}$$

$$\sigma_{eff}\frac{\partial \bar{T}}{\partial \bar{t}} + \bar{u}\frac{\partial \bar{T}}{\partial \bar{x}} + \bar{v}\frac{\partial \bar{T}}{\partial \bar{y}} = \alpha_{eff}\left[\frac{\partial^2 \bar{T}}{\partial \bar{x}^2} + \frac{\partial^2 \bar{T}}{\partial \bar{y}^2}\right] \tag{4}$$

where,

$$\begin{aligned}&F_C = \frac{1.75}{\sqrt{150\epsilon^3}}, K = \frac{{D_s}^2 \cdot \epsilon^3}{150(1-\epsilon)^2},\\ &\sigma_{eff} = \frac{\epsilon\left(\rho C_p\right)_{nf} + (1-\epsilon)\left(\rho C_p\right)_s}{\left(\rho C_p\right)_{nf}}, \alpha_{eff} = \frac{\epsilon k_{nf} + (1-\epsilon)k_s}{\left(\rho C_p\right)_{nf}}\end{aligned} \tag{5}$$

are denoted by the Forchheimer number, the permeability of the porous medium, the effective heat capacity ratio, and the effective thermal diffusivity, respectively, are defined as a function of the porosity (ϵ) of the porous medium. The subscripts 'nf' and 's' refer to the properties of nanofluids and the solid porous material, respectively. Furthermore, p is the pressure, θ is the temperature of the fluid, and D_s refers to the diameter of the porous particle. The values of ρ_{nf} and k_{nf} represent the NF's density and thermal conductivity, respectively. Here, μ_{eff} denotes the effective viscosity of the fluid medium under consideration. These variables and factors jointly regulate the system's flow and HT characteristics. On the right-hand side of the momentum equations Eq. (2)-(3), the viscous terms are arranged according to the order of Brinkman extension, Forcheimer extension, and Darcy model. The Brinkman term incorporates the viscous stresses introduced by the solid boundaries within the porous structure [52] while the Forchheimer term refers to the non-linear drag effect caused by the solid matrix in porous media [53]. In this model, the term $\frac{\bar{\mu}_{eff}}{K}v$ represents the Darcy term resulting from the friction caused by the porous matrix and the fluid medium. Combining these terms results in the Brinkman-Forchheimer extended Darcy model, which accounts for viscous and inertial terms.

2.4. Physical properties of nanofluids

The thermophysical properties of the base fluids (water), nanoparticles (Al_2O_3), and porous materials (solid Al) considered here are shown in Table 1. The properties include specific heat capacity (C_p), density (ρ), thermal conductivity (k), and thermal expansion coefficient (β).

The properties of nanofluids depend on various parameters, such as base fluid properties, particle dimensions and geometry, particle distribution, and fluid-particle interfacial effects. The effective density of the nanofluid (ρ_{nf}) can be calculated using the mixture rule, as shown in studies by [12].

$$\rho_{nf} = (1-\phi)\rho_f + \phi\rho_p, \tag{6}$$

where the subscripts 'f' and 'p' refer to the properties of the base fluid molecule and the nano-constituents, respectively. Furthermore, the specific heat $\left(C_p\right)_{nf}$ and thermal expansion (β_{nf}) of nanofluid can be calculated by the following mass averaging method [55].

$$\left(C_p\right)_{nf} = \frac{(1-\phi)\left(\rho C_p\right)_f + \phi\left(\rho C_p\right)_p}{\rho_{nf}}, \tag{7}$$

$$\beta_{nf} = \frac{(1-\phi)(\rho\beta)_f + \phi(\rho\beta)_p}{\rho_{nf}}. \tag{8}$$

The most important nanofluid properties in the context of HT study are the effective measurement of the thermal conductivity, which is crucial from the experimental perspective. According to the experimental model developed in [56], the effective thermal conductivity of the NF (k_{nf}) can be expressed as follows:

$$\frac{k_{nf}}{k_f} = 1 + \frac{k_p A p}{k_f A_f} + c\mathrm{Pe}\frac{k_p A_p}{k_f A_f} \quad \text{where} \quad \frac{A_p}{A_f} = \frac{d_f}{d_p}\frac{\phi}{(1-\phi)}. \tag{9}$$

In Eq. (9), the symbol $\mathrm{Pe} = \frac{u_p d_p}{\alpha_f}$ denotes the Peclet number corresponding to the Brownian velocity $u_p = \frac{2k_b T_0}{\pi\mu d_p^2}$ with $d_p = 47$ nm and $d_f = 0.384$ nm are, respectively, the nanoparticle and the water molecule diameter, Boltzman constant $K_b = 1.38 \times 10^{-23}$, and $c = 3.6 \times 10^4$. The thermophysical values for base fluid (water) and Al_2O_3 nanoparticles required in the above equations are adopted from Table 1.

Table 1
Thermophysical properties of base fluids and nanoparticles at $T_0 = 25\,°C$ [13,26,54].

Physical Properties	Base fluid	Nanoparticles	Porous Matrix
Specific heat capacity, C_p [J kg^{-1} K^{-1}]	4179	765	871
Viscosity, μ [Pa.s]	8.55×10^{-4}	0.324	-
Density, ρ [kg m^{-3}]	997.1	3970	2719
Thermal conductivity, k [W m^{-1} K^{-1}]	0.613	40	202.4
Thermal expansion coefficient, β [K^{-1}]	21×10^{-5}	0.85×10^{-5}	-

Table 2
The consistency parameter (m), power-law index (n) for characterizing the rheological behavior of non-Newtonian Al_2O_3-Water nanofluid at $T_0 = 25\,°C$ [25,26]. The associated Prandtl number (Pr) for the nanofluid is also provided, corresponding to $Re = 1000$.

ϕ (%)	0.0	0.5	1.0	1.5	2.0	2.5	3.0	3.5	4.0
m [N s^n m^{-2}]	0.0008554	0.00187	0.00230	0.00283	0.00347	0.00426	0.00535	0.00641	0.00750
n [-]	1	0.880	0.830	0.780	0.730	0.680	0.625	0.580	0.540
Pr_{nf} [-]	5.8315	9.8501	10.8807	12.0239	13.2408	14.5990	16.2903	17.7186	19.0237

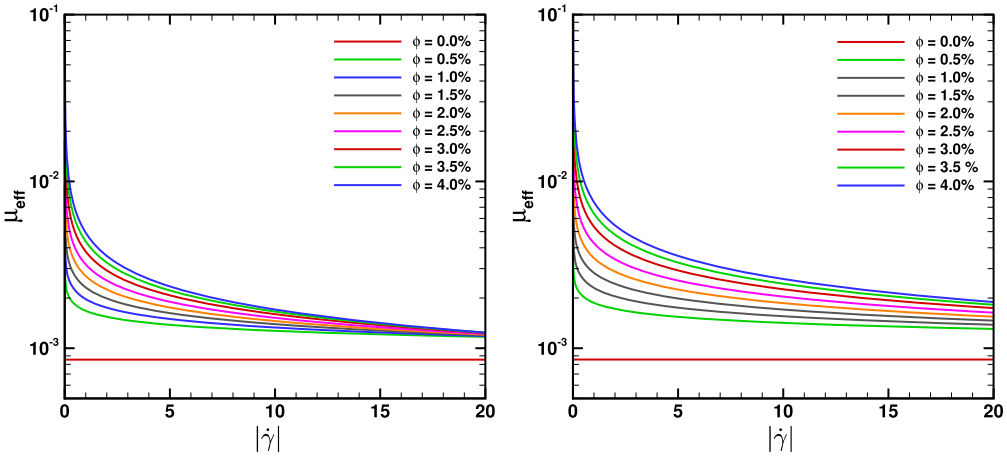

(a) $\epsilon = 0.4$ (b) $\epsilon = 0.99$

Fig. 2. Non-Newtonian viscosity (μ_{eff}) with respect to the applied shear rate ($|\dot{\gamma}|$) for the Al_2O_3-Water nanofluids for (a) $\epsilon = 0.4$ and (b) $\epsilon = 0.99$.

2.5. Power-law viscosity model for non-Darcy flow

In this study, we specifically consider aqueous solutions of Al_2O_3 nanofluids, whose effective dynamic viscosity has been experimentally observed as non-Newtonian shear thinning with respect to various nanoparticle concentrations (ϕ) and the operating temperature ($5\,°C \leq T \leq 45\,°C$) [24]. The reported results have been characterized by the non-Newtonian viscous power-law correlation for various types of nanofluids, such as Al_2O_3, CuO, and TiO_2 nanofluids. These observations exhibit the universality of the power-law model for correlating the rheological behavior of the nanofluid of interest used in the present study. Therefore, the effective viscosity (μ_{eff}) of the non-Newtonian nanofluid flowing through the porous medium has been attributed by the power-law viscosity model of the generalized non-Darcy flow [16],

$$\mu_{eff} = m|\dot{\gamma}|^{n-1} = m\left[\frac{1}{\epsilon}\sqrt{2\left(\frac{\partial \bar{u}}{\partial \bar{x}}\right)^2 + 2\left(\frac{\partial \bar{v}}{\partial \bar{y}}\right)^2 + \left(\frac{\partial \bar{u}}{\partial \bar{y}} + \frac{\partial \bar{v}}{\partial \bar{x}}\right)^2}\right]^{n-1} \tag{10}$$

where m, n and $\dot{\gamma}$ are crucial for characterizing non-Newtonian rheological properties. They are referred to as the consistency index, power-law index, and flow shear rate. The flow consistency parameter m [kg m^{-1} s^{n-2}] is contingent on the power-law index n. The effective viscosity of the non-Newtonian nanofluid differs from the Newtonian viscosity ($n = 1.0 \Rightarrow m = \mu_f = \mu_{eff}$). These differences are categorized into two types: shear-thinning fluids ($n < 1.0$) and shear-thickening fluids ($n > 1.0$). When the fluid exhibits shear-thinning properties, the viscosity decreases as the shear rate increases. This indicates that the fluid experiences less resistance to flow at higher shear rates, a common trait observed in complex fluids such as polymer solutions and suspensions. Conversely, shear-thickening fluids behave differently; their viscosity increases as the shear rate rises, indicating that they experience more resistance to flow with increasing shear rates.

Realizing the essentiality of the proper rheological characteristics of the naofluid considered in the present study, Table 2 presents the values for the m and n at various ϕ from the earlier experimental observations [25,26]. These parameters are essential for characterizing the non-Newtonian rheological behavior of the Al_2O_3-water NF, providing valuable insights into the fluid's non-Newtonian viscous behavior in response to the applied shear rate, which varies based on the weight percentage of suspended nanoparticles, as illustrated in Fig. 2. The figure depicts the predictive behavior of non-Newtonian rheology (μ_{eff} vs. $|\dot{\gamma}|$) of the nanofluid utilized in the present study within a porous medium in response to its different porous strength (e.g., $\epsilon = 0.4, 0.99$). The viscosity graphs illustrate that the effective viscosity decreases as porosity decreases when considering the applied shear rate for selected nanofluids. This phenomenon is significant when analyzing the convective HT rate of nanofluids in the non-Darcy regime within a porous medium.

Table 3
Input parameter ranges used in the numerical analysis [22,26,37,50,59].

Variables	Porosity (ϵ)	Volume fraction (ϕ)	Rayleigh number (Ra)	Reynolds number (Re)	Darcy number (Da)
Range	0.4 – 0.99	0% – 4%	10^5 - 10^6	300 – 1000	0.001 – 0.1

2.6. Governing equations in dimensionless form

Aiming for the numerical investigation for the present study, maintaining the simulation results free from the physical unit, the present study addresses the following dimensionless parameter [51,57,58].

$$x=\frac{\bar{x}}{H}, y=\frac{\bar{y}}{H}, u=\frac{\bar{u}}{U}, v=\frac{\bar{v}}{U}, \theta=\frac{T-T_C}{T_H-T_C}, t=\frac{\bar{t}U}{H}, P=\frac{\bar{p}}{\rho_f U^2},$$
$$Da=\frac{K}{H^2}, \lambda=\frac{\alpha_{eff}}{\alpha_f}, Re_{\mathrm{f}}=\frac{\rho_f U H}{\mu_f}, Pr_{\mathrm{f}}=\frac{\nu_f}{\alpha_f}=\frac{\mu_f (C_p)_f}{k_f},$$
$$Ra_{\mathrm{f}}=\frac{g\beta_f \Delta T D^3}{\nu_f \alpha_f}, Re_{\mathrm{nf}}=\left(\frac{H}{U}\right)^{n-1}\frac{\mu_f}{m}Re_{\mathrm{f}}, Pr_{\mathrm{nf}}=\left(\frac{H}{U}\right)^{1-n}\frac{m}{\mu_f}Pr_{\mathrm{f}},$$
$$Ra_{\mathrm{nf}}=\left(\frac{H}{U}\right)^{n-1}\frac{\mu_f}{m}Ra_{\mathrm{f}}, Ri=\frac{Ra_{\mathrm{nf}}}{Pr_{\mathrm{nf}}Re_{\mathrm{nf}}^2}=\frac{Ra_{\mathrm{f}}}{Pr_{\mathrm{f}}Re_{\mathrm{f}}^2}, Re_{\mathrm{nf}}Pr_{\mathrm{nf}}=Re_{\mathrm{f}}Pr_{\mathrm{f}},$$
$$\eta=\frac{1}{\epsilon^{n-1}}\left[2\left(\frac{\partial u}{\partial x}\right)^2+2\left(\frac{\partial v}{\partial y}\right)^2+\left(\frac{\partial u}{\partial y}+\frac{\partial v}{\partial x}\right)^2\right]^{\frac{n-1}{2}} \tag{11}$$

In the above equation, the symbol () represents dimensional variables, υ_f and α_f denote the kinematic viscosity and the thermal diffusivity of the base fluid, while u and v represent the fluid velocities along the x and y directions. The parameter η refers to the dimensionless shear rate. Additionally, Pr_f, Ra_f, and Re_f are used to denote the Prandtl number, Rayleigh number, and Reynolds number for the base-fluid, respectively. The following Table 3 provides the range of values used for various dimensionless parameters and physical properties in a fluid dynamics and heat transfer study that likely involves porous media and nanofluid flow. Here, ϵ values are selected in the range 0.4–0.99 to represent realistic porous materials such as metallic foams, fibrous media, and packed beds, which are commonly used in thermal management applications [50]; Da values span 0.001 to 0.1 to account for both high- and low-permeability porous media, capturing transitions from Darcy to Forchheimer flow regimes, as seen in insulation materials and geothermal reservoirs [59]; ϕ values are limited to 0–4% by showing shear-thinning rheology, to ensure the stability of the nanofluid, avoid agglomeration, and maintain the accuracy of the single-phase model [22,26]; Re values are selected to capture laminar flow regimes, addressing the applications in microchannels, heat exchangers, and biomedical devices [37]; Ra values are chosen to represent regimes with significant natural convection and buoyancy forces, especially in porous enclosures and vertical cavities [50,59].

After employing the above transformations in Eq. (11), the governing equations in non-dimensional form are obtained by,

$$\frac{\partial u}{\partial x}+\frac{\partial v}{\partial y}=0 \tag{12}$$

$$\frac{\rho_{nf}}{\rho_f}\left[\frac{1}{\epsilon}\frac{\partial u}{\partial t}+\frac{1}{\epsilon^2}u\frac{\partial u}{\partial x}+\frac{1}{\epsilon^2}v\frac{\partial u}{\partial y}\right]$$
$$=-\frac{\partial p}{\partial x}+\frac{1}{Re_{nf}}\left[\frac{1}{\epsilon}\frac{\partial}{\partial x}\left(2\eta\frac{\partial u}{\partial x}\right)+\frac{1}{\epsilon}\frac{\partial}{\partial y}\left(\eta\frac{\partial u}{\partial y}+\eta\frac{\partial v}{\partial x}\right)-\frac{\eta}{Da}u\right]$$
$$-\frac{F}{\sqrt{Da}}u\sqrt{u^2+v^2} \tag{13}$$

$$\frac{\rho_{nf}}{\rho_f}\left[\frac{1}{\epsilon}\frac{\partial v}{\partial t}+\frac{1}{\epsilon^2}u\frac{\partial v}{\partial x}+\frac{1}{\epsilon^2}v\frac{\partial v}{\partial y}\right]$$
$$=-\frac{\partial p}{\partial y}+\frac{1}{Re_{nf}}\left[\frac{1}{\epsilon}\frac{\partial}{\partial x}\left(\eta\frac{\partial v}{\partial x}+\eta\frac{\partial u}{\partial y}\right)+\frac{1}{\epsilon}\frac{\partial}{\partial y}\left(2\eta\frac{\partial v}{\partial y}\right)-\frac{\eta}{Da}v\right]$$
$$-\frac{F}{\sqrt{Da}}v\sqrt{u^2+v^2}+\frac{Ra_{nf}}{Pr_{nf}.Re_{nf}{}^2}\theta \tag{14}$$

$$\sigma_{eff}\frac{\partial\theta}{\partial t}+u\frac{\partial\theta}{\partial x}+v\frac{\partial\theta}{\partial y}=\frac{\lambda}{Re_{nf}Pr_{nf}}\left(\frac{\partial^2\theta}{\partial x^2}+\frac{\partial^2\theta}{\partial y^2}\right) \tag{15}$$

The non-dimensional boundary conditions associated with the BFS flow are given by

$$\text{when } t=0, \quad u=v=\theta=0, \quad \forall x,y \tag{16}$$

$$\text{when } t>0 \begin{cases} \text{At the channel inlet:} & u(y)=12(3y-2y^2-1), \quad \theta(y)=0 \\ \text{At the channel outlet:} & \frac{\partial u}{\partial x}=\frac{\partial v}{\partial x}=\frac{\partial\theta}{\partial x}=0 \\ \text{At the top wall:} & u=v=\theta=0 \\ \text{At the bottom downstream wall:} & u=v=0, \quad \theta=1 \\ \text{At the step wall:} & u=v=0, \quad \frac{\partial\theta}{\partial x}=0 \end{cases} \tag{17}$$

2.7. Heat transfer (HT) rate

The local Nu number and the Nu_{avg} number are defined in the following to measure the HT performance,

$$Nu=-\frac{k_{nf}}{k_f}\left(\frac{\partial\theta}{\partial y}\right)_{\text{heated wall}}, \quad Nu_{\text{avg}}=\frac{1}{l_w}\int_{\text{heated wall}} Nu\,\mathrm{d}s \tag{18}$$

where ds indicates the differential element along the heated wall and l_w is the length of the heated wall. To evaluate the increase in HT resulting from the addition of nanoparticles, we introduced the E% parameter [57], which measures the rise in the Nu_{avg} as,

$$E\%=\frac{Nu_{avg}(\phi)-Nu_{avg}(\phi=0.0)}{Nu_{avg}(\phi=0.0)}\times 100 \tag{19}$$

2.8. Entropy generation (EGEN)

According to the second law of thermodynamics, any real-world HT process involves a change in entropy because natural processes are irreversible. Entropy is defined by the quantitative measurement of energy loss in any natural phenomenon [60]. The change in entropy in the convective HT process is contributed by fluid friction (FF) and the HT mechanism [61]. The dimensional forms for EGEN due to FF and HT in non-Newtonian NF flow through a porous medium are denoted by $\bar{S}_{ff}$ and $\bar{S}_{HT}$ respectively, with the following definition [57],

$$\bar{S}_{ff}=\frac{\mu_{eff}}{T_0}\left[\frac{\bar{u}^2+\bar{v}^2}{K}+2\left(\frac{\partial\bar{u}}{\partial\bar{x}}\right)^2+2\left(\frac{\partial\bar{v}}{\partial\bar{y}}\right)^2+\left(\frac{\partial\bar{u}}{\partial\bar{y}}+\frac{\partial\bar{v}}{\partial\bar{x}}\right)^2\right] \tag{20}$$

$$\bar{S}_{HT}=\frac{k_{nf}}{T_0^2}\left[\left(\frac{\partial\bar{T}}{\partial\bar{x}}\right)^2+\left(\frac{\partial\bar{T}}{\partial\bar{y}}\right)^2\right] \tag{21}$$

The non-dimensional form of the above quantities is then derived by,

$$S_{ff}=\left[\frac{T_0^2H^2}{k_f(\Delta T)^2}\right]\bar{S}_{ff}$$
$$=\lambda_1\frac{mU^{n+1}}{\mu_f H^{n+1}}\eta\left[\frac{u^2+v^2}{Da}+2\left(\frac{\partial u}{\partial x}\right)^2+2\left(\frac{\partial v}{\partial y}\right)^2+\left(\frac{\partial u}{\partial y}+\frac{\partial v}{\partial x}\right)^2\right] \tag{22}$$

$$S_{HT}=\left[\frac{T_0^2H^2}{k_f(\Delta T)^2}\right]\bar{S}_{HT}=\frac{k_{nf}}{k_f}\left[\left(\frac{\partial T}{\partial x}\right)^2+\left(\frac{\partial T}{\partial y}\right)^2\right] \tag{23}$$

Table 4
Comparison of Nu_{avg} for the various grid dimensions for $Re = 1000$ at $\phi = 0.00$ ($n = 0$), and 0.04 ($n = 0.54$) for Al_2O_3-water nanofluid flowing through a porous medium with different strength $\epsilon = 0.4$, 0.99.

Number of elements	Nu_{avg} ($\|\Delta\|$%)			
	$\epsilon = 0.4$		$\epsilon = 0.99$	
	$\phi = 0.00$	$\phi = 0.04$	$\phi = 0.00$	$\phi = 0.04$
$G_1 = 20,000$	33.809 (0.01%)	34.334 (0.02%)	2.990 (0.10%)	3.314 (0.06%)
$G_2 = 40,000$	33.806 (0.00%)	34.328 (0.00%)	2.987 (0.00%)	3.312 (0.00%)
$G_3 = 80,000$	33.807 (0.006%)	34.331 (0.01%)	2.988 (0.03%)	3.313 (0.03%)

where the parameter $\lambda_1 = \frac{\mu_f T_0 H^2}{k_f (\Delta T)^2}$ is referred to as the irreversibility distribution ratio [62], which is defined as the ratio between viscous and HT irreversibility [63].

2.9. Performance evaluation criteria (PEC)

Nanofluids have become popular in thermal systems engineering because of their ability to enhance energy exchange from a thermal system by offering superior thermal conductivity. However, introducing nanoparticles into the base fluid increases the viscosity, leading to a higher pressure drop and elevated operational expenses due to the additional pumping power required [64]. To reckon the effectiveness of nanofluids in thermal engineering systems, a criterion known as the Performance Evaluation Criterion (PEC) has been established in the experimental community. The PEC is defined as the ratio of the HT rate to the required pumping power in the system:

$$PEC = \frac{h_{nf}/h_{bf}}{\Delta P_{nf}/\Delta P_{bf}} \tag{24}$$

where $\Delta P = \overline{P_i} - \overline{P_o}$ represents the pressure drop with $\overline{P_i}$ and $\overline{P_o}$ denote the average inlet and outlet pressure, respectively, in a fluid system and h denotes the HT coefficient. Higher values of PEC suggest the suitability of utilizing nanofluids in a thermal system for HT improvement. The criterion offers a comprehensive measure of the overall benefit of nanoparticles, considering both improved HT properties and the energy required for fluid flow. This investigation considers the potential real-world uses of NFs by investigating the impact of increased HT and pressure drop. The HT rate of NFs increases because of their higher thermal conductivity, leading to a rise in pressure drop due to increased viscosity.

3. Numerical implementation

3.1. Numerical method

A custom numerical code written in the FORTRAN programming language implements the finite volume numerical method (FVM) to provide numerical solutions for the dimensionless governing equations outlined in Eqs. (12)-(15). The boundary conditions listed in Eqs. (16)-(17) are incorporated into the code, which performs double-precision calculations. As per 2D-FVM technique, this method assumes a finite number of control volumes (CVs) within the solution domain. Each control volume consists of four faces—east, south, west, and north—along with a center node where the flow variable computations are performed. This method discretizes the dimensionless partial differential equations across these control volumes. The mesh distribution within the solution domain is designed to be denser near the walls and sparser further away, allowing for an accurate representation of the complex fluid interactions within a thin boundary [51]. This enhances the accuracy of the numerical simulations throughout the entire computational process. The simulation proceeds with an invariant time step $\Delta t = 10^{-5}$, employing a three-point backward difference method for temporal advancement. A second-order central-difference technique is utilized to discretize the convective and diffusion terms. The well-established SIMPLE (Semi-Implicit Method for Pressure-Linked Equations) algorithm is implemented to couple velocity and pressure within the momentum equations during the iterative process. To ensure convergence, the relative errors in the field variables (u, v, and θ) between consecutive iterations must remain below 10^{-6}. A collocated grid arrangement is adopted, and Rhie–Chow interpolation is used to avoid pressure–velocity decoupling. The discretized linear systems for velocity and energy equations are solved using the Bi-Conjugate Gradient Stabilized (Bi-CGSTAB) method, while the pressure correction equation in SIMPLE is solved via the Incomplete Cholesky Conjugate Gradient Method (ICCGM). The simulation continues until a steady state is achieved, which is confirmed when the residuals for all variables drop below 10^{-6} and show no further change over successive time steps. More details of the numerical framework are also available in [47,65]. The following sections will cover grid independence tests and code validation to ensure the accuracy and reliability of the numerical methods in this study. The numerical framework is validated by comparing results with benchmark cases for backward-facing step flow and porous channel convection, as discussed in Section 3.3.

3.2. Grid sensitivity test

A grid-sensitivity test was conducted to validate the accuracy and consistency of the simulation. Various grid sizes were tested while maintaining constant values for other parameters. The simulation parameters included $Re = 1000$, $Da = 0.1$, $Ra = 10^6$, $\phi = 0.00$ ($n = 0$), and 0.04 ($n = 0.54$). Additionally, different porous strengths, $\epsilon = 0.4$ and $\epsilon = 0.99$, of the porous medium were tested. The primary objective was to determine the most appropriate grid size. The study employed a rectangular mesh with three different grid sizes: 20,000, 40,000, and 80,000 elements. The detailed findings are presented in Table 4. After comparison, a grid size of G_2 (consisting of 40,000 elements) was selected, providing a good balance between high accuracy and computational efficiency. The values in brackets indicate the absolute error percentage between G_2 and the other grid sizes.

3.3. Numerical validation

In this section, we have thoroughly validated the code by comparing current numerical findings against experimental data and established benchmark numerical solutions. The core element is validation, intended to assess how well our model captures the intricate flow and heat transfer phenomena post-step region.

3.3.1. Experimental validation

Fig. 3 illustrates a comparison between the current numerical results and benchmark experimental findings on precise velocity profile measurements at various points ($X_R(=\bar{x})/h$) along the upstream and downstream steps for $Re = 1095$, as reported by Armaly et al. [35], showing an excellent match. It is evident that the velocity profile before the step, at $X_R/h = -1.76$, is parabolic within the laminar regime. The velocity profiles indicate that the flow separates at the step, forming one, two, or three recirculation zones after the step, eventually re-establishing a fully developed parabolic velocity profile in the wider channel.

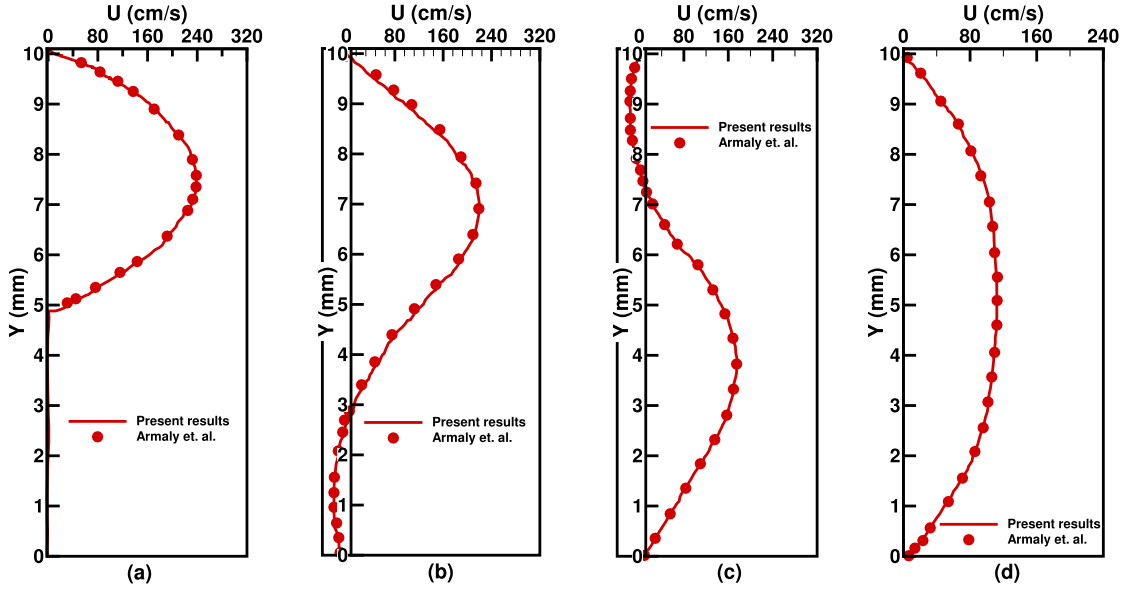

Fig. 3. Validation of Velocity profiles within a BFS configuration for Re = 1095 at different locations (a) $X_R/h = -1.76$, (b) $X_R/h = 7.04$, (c) $X_R/h = 19.04$, and (d) $X_R/h = 67.44$ as experimentally reported by Armaly et al. [35].

Table 5
Comparison of the reattachment length (X_R/h) between Present result with M. M. Molla [66] and Erturk [37] for various Power-law Indexes (n) and *Re* Numbers.

Re	$n = 0.5$		$n = 0.8$		$n = 1.0$		$n = 1.2$		$n = 1.5$	
	Present	in [66]	Present	in [66]	Present	in [37]	Present	in [66]	Present	in [66]
100	4.234	4.501	3.410	3.512	2.922	2.922	2.477	2.539	1.962	1.943
200	7.608	8.171	5.924	6.032	4.987	4.982	4.160	4.213	3.201	3.229
300	10.648	-	8.111	7.332	6.743	6.751	5.619	5.853	4.283	4.530
400	13.451	-	9.971	-	8.191	8.237	6.846	6.974	5.239	5.412

Table 6
Comparison of Nu_{avg} between present result and results reported by Nithiarasu [50] and G. Lauriat and V. Prasad [59] for different porosity (ϵ), permeability (Da), and Buoyancy strength (Ra).

Da	*Ra*	Present			Nithiarasu [50]			G. Lauriat and V. Prasad [59]	
		$\epsilon = 0.4$	$\epsilon = 0.6$	$\epsilon = 0.9$	$\epsilon = 0.4$	$\epsilon = 0.6$	$\epsilon = 0.9$	$\epsilon = 0.4$	$\epsilon = 0.9$
10^{-6}	10^7	1.07	1.07	1.07	1.079	1.079	1.08	1.07	1.07
	10^8	3.05	3.07	3.08	2.97	2.997	3.00	3.07	3.09
10^{-4}	10^5	1.06	1.06	1.06	1.067	1.071	1.072	1.07	1.07
	10^6	2.59	2.70	2.79	2.55	2.725	2.740	2.97	3.05
10^{-2}	10^3	1.01	1.01	1.01	1.01	1.015	1.023	1.06	1.06
	10^4	1.36	1.49	1.63	1.408	1.530	1.64	2.28	2.67

3.3.2. Numerical validation for reattachment length

Another validation has been established in Table 5, which focuses on different *Re* and power-law index (n), highlighting the reattachment length of the bottom wall. This table provides a comprehensive insight into how varying combinations of *Re* and n impact the flow dynamics, offering a crucial understanding of the hydrodynamic behavior in terms of the reattachment length within the BFS configuration. Increasing *Re* numbers influence the separation and reattachment points. Higher *Re* numbers generally result in longer reattachment lengths due to increased momentum effects in the flow. The symbol n characterizes the rheological nature of the medium, representing different degrees of shear-thinning or shear-thickening behavior. Lower values of the $n = 0.5$ indicate more pronounced shear-thinning behavior, potentially affecting separation and reattachment characteristics. As n increases, reflecting more viscous resistance, the flow may exhibit more stable and predictable reattachment lengths. By comparing these findings with existing results [37,66], we can gain insights into the consistency of results across different studies. Differences or similarities in reattachment lengths can indicate the robustness of observed phenomena and the reliability of numerical simulations or experimental data.

3.3.3. Numerical validation for different porous media with porosity

Table 6 presents the validation results for a diverse range of *Da* and *Ra* numbers, focusing specifically on porous media by considering different porous strengths ($\epsilon = 0.4$, 0.6, and 0.9) and exploring different combinations of *Da* and *Ra* numbers. The table offers a deeper understanding of how porous media influence energy transfer (Nu_{avg}) within a thermal system. The comparison of Nu_{avg} with different *Da* values illustrates the impact of porous medium permeability on convective HT, where lower *Da* values generally indicate higher convective HT rates. Additionally, the influence of the *Ra* values on the Nu_{avg} is explored, considering that variations in *Ra* can significantly affect convective HT due to the fluid's buoyancy-driven flow and thermal gradients. Results are presented for three different values of the Forchheimer parameter,

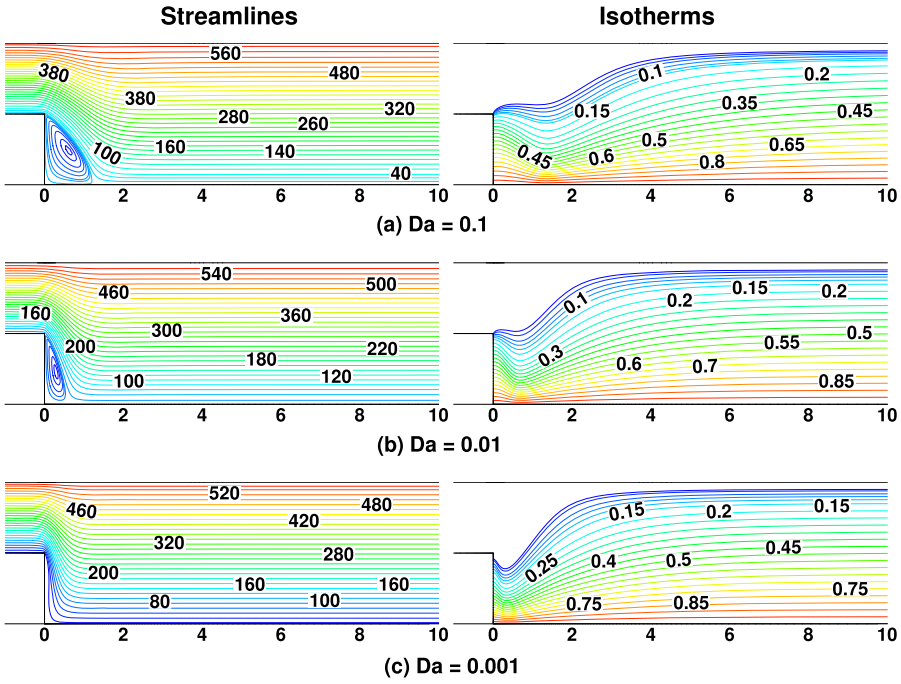

Fig. 4. Effects of $Re = 1000$ numbers on the Streamlines and Isotherms at $Ra = 10^6$, $\phi = 0.04$, and $\epsilon = 0.4$.

ϵ, which characterizes the deviation from Darcy's law in porous media and represents the extent of inertial effects on fluid flow through the porous medium and also includes a comparison with results from two other studies [50,59] to validate the present findings against established research. Within each set of Da and Ra values, the Nu_{avg} numbers are presented for varying values of ϵ, offering insights into how changes in the Forchheimer parameter influence convective HT within the porous medium. Overall, the validation trials confirm the accuracy of the numerical system in capturing complex fluid dynamics and HT in the BFS.

4. Results and discussion

This paper examines simulations to study the flow dynamics of a non-Newtonian NF in an abruptly widened porous channel, taking into account different Reynolds (Re), Darcy (Da), and Rayleigh (Ra) numbers, as well as varying porous strengths from $\epsilon = 0.4$ to 0.99 and the percentage of nanoparticle presence (ϕ). It was found that when the Re number escalates, the recirculation zone diminishes in size for identical Ra values but with varied ϕ levels. This investigation delves into the innovative use of non-Newtonian NFs within a homogeneous porous medium exhibiting non-Darcian effects. The computations are further dissected in the following sections, focusing on streamlines, isotherms, skin friction coefficient, recirculation region extent, average Nusselt number (Nu_{avg}), Nu enhancement, and entropy generation. This analysis encompasses several key parameters, such as nanoparticle volume fraction ($\phi = 0\%$ to 4%), Darcy number ($Da = 0.1$, 0.01, 0.001), Rayleigh number ($Ra = 10^5$, 10^6), skin friction coefficient (C_f), and entropy generation metrics (S_{ff} and S_{HT}).

4.1. Streamlines and isotherms analysis

In this section, we investigate the behavior of fluid flow under various parameters. Figs. 4 and 5 illustrate the impact of a constant Re number ($Re = 1000$) on the HT characteristics of non-Newtonian Al_2O_3-water NFs. When $Ri \ll 1$, forced convection dominates, indicating that external forces primarily drive the flow. In contrast, when $Ri \gg 1$, natural convection dominates, which means that buoyancy effects are the primary driver of flow. When $Ri \approx 1$, mixed convection occurs, where both the buoyancy and the shear forces are equally significant. The study investigates Ri numbers ($Ri = 0.171$) while maintaining a constant Ra value of 10^6 and also focuses on the impact of forced convection.

The response of streamlines and isotherms has been observed for the non-Newtonian nanofluid with shear thinning behavior associated with a choice of $\phi = 0.04$, $m = 0.007500$, and $n = 0.54$ while varying $Da = 0.1$, 0.01, and 0.001, and $\epsilon = 0.4$ and 0.9. Fig. 4 illustrates the effect of the Da number on streamlines and isotherms for a $Re = 1000$ in a porous medium, which suggests forced convection is dominant in the flow. The Da number measures the relative permeability of the medium, significantly influencing the flow patterns and HT mechanisms. The streamlines show the flow patterns at different Da numbers within a channel. At a high Da number ($Da = 0.1$), the medium's permeability is high, allowing the fluid to flow with less resistance. The streamlines after the steps exhibit the presence of a recirculation region, thus resulting in a weak HT rate from the downstream wall. The isotherms show widely spaced temperature contours, indicating efficient convective HT, as the freely moving fluid enhances HT across the domain. As the Da number decreases to $Da = 0.01$, the flow encounters increased resistance due to reduced permeability, leading to less pronounced recirculation after the step. The isotherms depict steeper temperature gradients, signaling a gradual shift towards conduction-dominated HT as the flow resistance intensifies. At a low Da number ($Da = 0.001$), the flow experiences significant resistance due to the weak permeability of the porous structure, resulting in very weakly pronounced recirculation zones and tightly packed streamlines. In this scenario, the isotherms exhibit even steeper temperature gradients, reflecting conduction-dominated HT, as the slow-moving fluid limits the efficiency of convective transport. The transition from $Da = 0.1$ to $Da = 0.001$ illustrates a shift from convection-dominated to conduction-dominated HT, emphasizing how decreasing permeability increases flow resistance, restricts fluid movement, and alters the balance between convective and conductive HT within the porous medium. Fig. 5 presents the effects of varying $Da = 0.1$, 0.01, and 0.001 on the streamlines and isotherms for a flow configuration at $Re = 1000$, $Ra = 10^6$, $\phi = 0.04$, $\epsilon = 0.9$ compared to the stronger porous medium as seen in Fig. 4. Results show that for $Da = 0.001$, the flow appears slower through a low permeability medium, as indicated by widely spaced streamlines, suggesting less resistance from the porous medium and faster flow reattachment af-

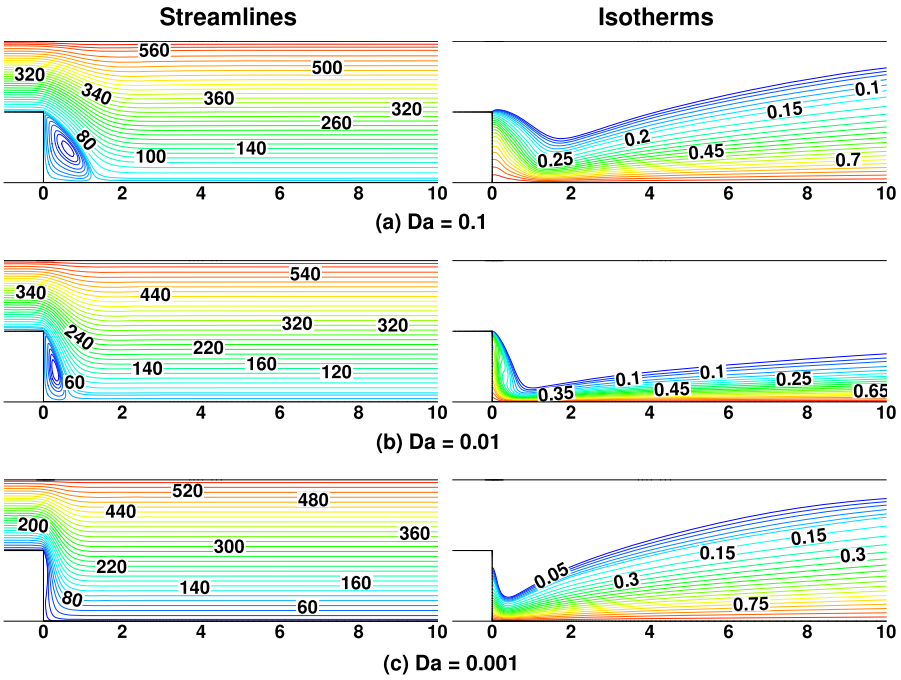

Fig. 5. Effects of $Re = 1000$ numbers on the Streamlines and Isotherms at $Ra = 10^6$, $\phi = 0.04$, and $\epsilon = 0.9$.

ter separation. A noticeable recirculation region forms near the BFS, but the flow swiftly adjusts downstream. The temperature distribution is relatively smooth with gradual thermal gradients, reflecting efficient HT across the domain. In the case of $Da = 0.01$, the porous permeability increases, resulting in more compact streamlines. The recirculation zone becomes more pronounced, and the flow takes longer to reattach, indicating a more obstructed flow pattern, requiring higher energy to overcome the increased resistance. The isotherms become more compressed near the step, showing rising thermal resistance. HT becomes less efficient, and heat takes longer to diffuse across the domain, especially near the recirculation region. For $Da = 0.1$, the flow experiences less significant resistance from the porous medium, leading to highly compact streamlines and a more localized recirculation zone. The flow experiences considerable difficulty in reattaching, indicating powerful obstruction of fluid motion by the porous medium. The isotherms show sharp thermal gradients, with further compression indicating reduced thermal diffusion. The flow's capacity to transfer heat is greatly diminished due to the porous medium, resulting in strong resistance to both the flow and HT mechanisms.

4.2. Skin-friction effect analysis (C_f)

In association with the BFS flow, a major component for investigation involves evaluating the wall shear stress or local skin friction coefficient (C_f). In the Fig. 6, investigations conceive the C_f at the lower wall for different $\phi = 0\%$ to 4% with different Da numbers ($Da = 0.1$, 0.01, and 0.001), Re numbers ($Re = 500$ and 1000), Ra number ($Ra = 10^6$), and the porosity ($\epsilon = 0.4$, and 0.9). These parameters significantly impact flow characteristics due to the complex fluid dynamics associated with the porous medium. As illustrated in Fig. 6, the wall shear stress on the downstream wall exhibits noticeable variations. Exceptions occur after the step wall, where $C_f \leq 0$ due to negative velocity in association with the recirculation fluid domain. After the flow reattachment, with the increase in ϕ, C_f increases positively for all the cases of $Da = 0.1$, 0.01, and 0.001. With an increase in ϕ, C_f becomes stronger in a negative direction within the recirculation zone. For shear-thinning fluids ($\phi = 0.0$ to 0.04 and $n < 1.0$), C_f grows stronger in the positive direction when the flow is reattached to the wall than for the case of $n = 1.0$. In the case of $Re = 500$, we observe a noticeable increase in C_f as Da decreases from 0.1 to 0.001. The reduced permeability associated with lower Da leads to increased flow resistance within the porous medium, resulting in higher skin friction coefficients. This is because the flow encounters more resistance as it moves through the porous structure, requiring elevated shear stress to maintain the same flow rate. Additionally, an increase in nanoparticle volume fractions leads to higher fluid viscosity due to suspended particles, further contributing to the augmentation of C_f. The interaction between increased viscosity and reduced permeability results in a non-linear escalation in friction, highlighting the complex relationship between the solid porous media and the liquid nanofluid media. Similar trends are evident in case (b); however, the skin-friction coefficient C_f exhibits lower values than those observed at $Re = 500$. This is primarily due to the more pronounced inertial effects dominating the flow behavior at higher Re numbers. Elevated Re numbers lead to a greater inertial force than viscous forces, reducing the frictional effects seen under lower Re conditions. As Da decreases, the continuous increase in flow resistance within the less permeable porous medium continues to elevate C_f, although with less pronounced effects than those observed in the lower Re number case. In case (c), for $Re = 1000$ and $\epsilon = 0.9$, the inertial forces become more dominant due to the higher flow velocity and porosity. The increase in Re causes steeper velocity gradients near the wall, resulting in higher wall shear stress compared to $Re = 500$. Consequently, the C_f is generally higher in $Re = 1000$ than in $Re = 500$. Similarly to the previous case, at $Da = 0.1$, the porous medium offers less resistance, and the skin friction remains relatively low. However, as the Da number decreases to $Da = 0.01$ and $Da = 0.001$, the reduction in permeability amplifies the shear forces in the wall, significantly increasing C_f. At higher nanoparticle concentrations, the increase in viscosity due to the presence of nanoparticles further enhances the wall shear stress, particularly at $Re = 1000$, where the higher flow velocities exacerbate the effects of viscous forces.

4.3. Recirculation length analysis

The present study aims to investigate how the reattachment length changes due to the variation of permeability, inertia forces, volume fraction, buoyancy forces, and porosity. The reattachment length is the distance from the point where the flow resumes in the forward direction across the entire cross-section. It is an important parameter in fluid

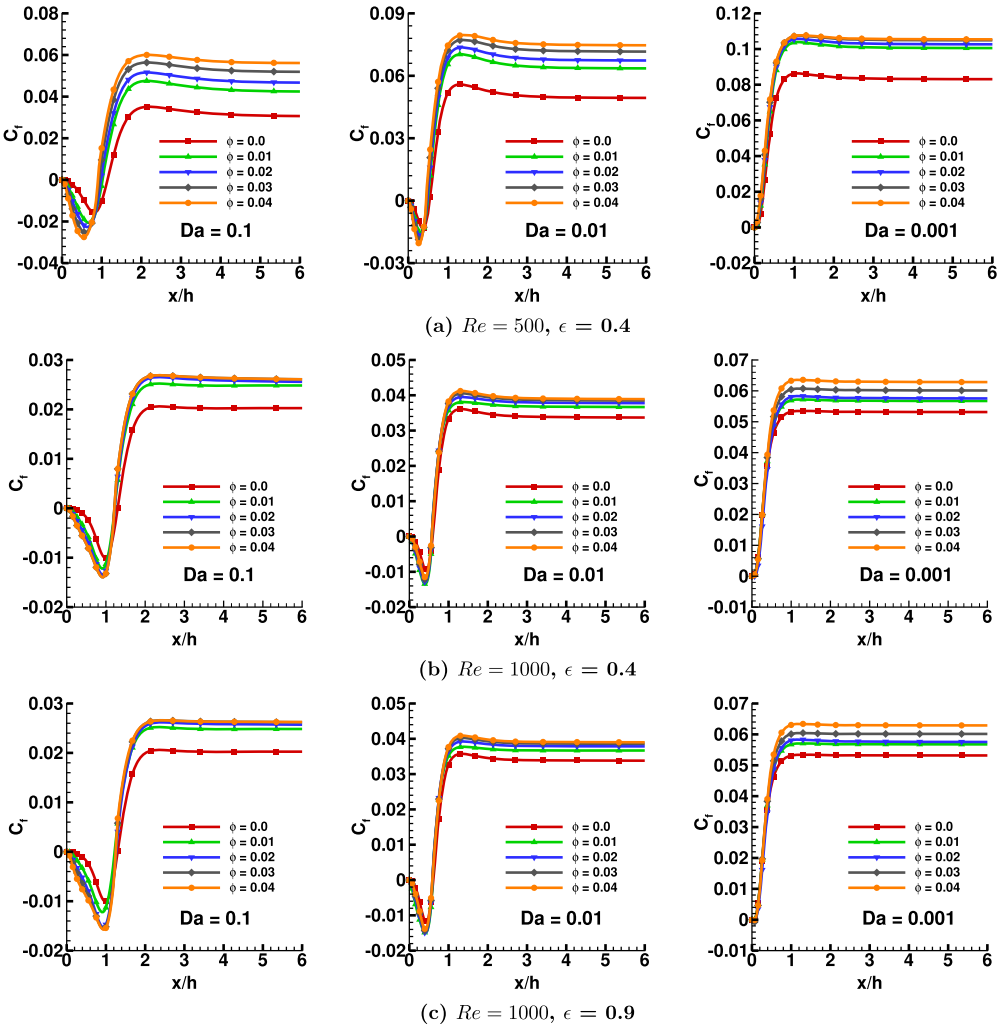

Fig. 6. Skin-friction coefficient, $C_f = \tau_w / \frac{1}{2}\rho_0 U^2$ at the lower wall for the different values of ϕ at (a) Re = 500, (b) Re = 1000 while $Da = 0.1, 0.01, 0.001$. $Ra = 10^6$ and $\epsilon = 0.4$.

dynamics, indicating the point where separated flow reattaches to a surface. The study focuses on recirculation areas along the bottom wall, which play a critical role in fluid mixing and HT efficiency. The research tackles the significance of understanding fluid flow characteristics and HT phenomena in porous media, particularly in non-Newtonian NF systems. By examining the influence of parameters such as Da, Re, Ra, ϕ, and ϵ, the study aims to offer insights into optimizing HT processes in porous media. The flow characteristics are more clearly visualized through streamlines, as depicted in Figs. 4 and 5. These figures reveal a distinct secondary flow within the recirculation region formed in the separated corner.

In Fig. 7, the reattachment length (X_s) of the bottom wall's recirculation region is depicted for various Darcy numbers ($Da = 0.1, 0.01, 0.001$), Reynolds numbers ($Re = 300 - 1000$), and $\phi = 0\%$ to 4% at a constant Rayleigh number ($Ra = 10^6$). Two porosity values ($\epsilon = 0.4$ and $\epsilon = 0.9$) are considered to analyze the impact of porosity on the flow and reattachment behavior. In scenario (a), a decrease in Da from 0.1 to 0.001 leads to a noticeable reduction in X_s. A lower Da indicates a more restrictive porous medium, resulting in higher flow resistance and a shrinking recirculation region due to lower permeability hindering extensive fluid reattachment. However, higher Reynolds numbers ($Re = 1000$) result in longer reattachment lengths due to stronger inertial forces. The increased fluid momentum at higher Re sustains the recirculation zone over a longer distance. Furthermore, an increase in ϕ causes a decrease in X_s. As ϕ increases, the fluid's viscosity rises, dampening the nanofluid's motion and leading to reduced recirculation as the flow stabilizes more quickly. In scenario (b), the higher porosity allows for a more pronounced flow behavior. Similar trends are observed, with X_s decreasing with lower Da and higher ϕ, while higher Re tends to extend the reattachment length. The high porosity permits greater fluid flow through the medium. Nevertheless, the overall impact of Re and ϕ remains consistent: larger Re enhances fluid inertia, promoting longer reattachment zones, and increasing ϕ increases viscosity, leading to more stable, less recirculated flows.

4.4. Average HT rate (Nu_{avg})

In Table 7, the impact of varying porosity (ϵ) on Nu_{avg} within the framework of the Brinkman-Forchheimer model is presented. The study explores different combinations of porosity, nanoparticle volume fraction (ϕ), Da number, and Re number while maintaining a constant $Ra = 10^6$. It is found that as porosity increases, Nu_{avg} consistently decreases across all scenarios. Higher porosity, typically associated with increased fluid flow in natural convection, leads to reduced HT efficiency in porous media due to decreased solid-fluid interaction and increased influence of inertial forces, as modeled by the Brinkman-Forchheimer approach. Furthermore, an increase in ϕ from 0% to 4% results in a slight increase in the average Nu number, particularly at lower porosity values. This suggests that nanoparticles enhance the thermal conductivity of the fluid, thereby improving HT despite the decline caused by increasing porosity. Moreover, combining higher nanoparticle concentration with lower porosity enhances HT more than either factor

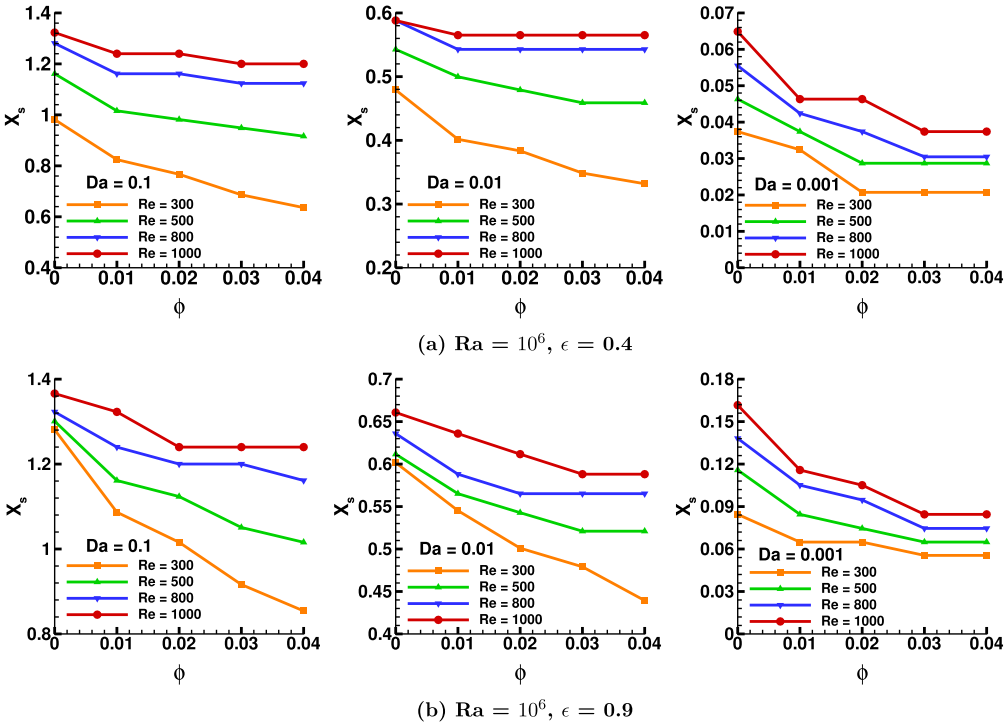

Fig. 7. Length of the bottom wall's recirculation regions for Da numbers with incrementing Re for constant $Ra = 10^6$ number and various ϕ and Da while $\epsilon = 0.4$ and 0.9.

Table 7
The average Nusselt number (Nu_{avg}) with respect to varying ϕ incorporating the changes in ϵ and Da numbers for the Brinkman - Forchheimer model while $Ra = 10^6$.

Re	Da	Ri	$\epsilon = 0.4$	$\epsilon = 0.5$	$\epsilon = 0.6$	$\epsilon = 0.7$	$\epsilon = 0.8$	$\epsilon = 0.9$	$\epsilon = 0.99$
$\phi = 0\%$									
	0.1		31.611	26.754	21.902	17.055	12.211	7.368	2.321
500	0.01	0.686	31.425	26.672	21.729	16.896	12.078	7.276	2.251
	0.001		31.355	26.501	21.657	16.824	12.006	7.208	2.150
	0.1		33.806	29.181	24.329	19.479	14.626	9.668	2.987
1000	0.01	0.172	33.778	28.964	24.135	19.457	14.490	9.559	2.742
	0.001		33.649	28.928	24.073	19.228	14.390	9.377	2.587
$\phi = 4\%$									
	0.1		31.875	27.025	22.181	17.341	12.505	7.667	2.546
500	0.01	0.686	31.754	26.908	22.069	17.237	12.413	7.593	2.459
	0.001		31.615	26.771	21.935	17.111	12.299	7.501	2.355
	0.1		34.328	29.735	24.889	20.045	15.194	10.197	3.312
1000	0.01	0.172	34.185	29.501	24.680	19.864	15.046	10.074	3.289
	0.001		34.008	29.200	24.402	19.615	14.831	9.881	3.167

alone. Additionally, higher Da numbers ($Da = 0.1$) correspond to higher permeability, allowing more fluid to flow through the medium, thus increasing convective HT. Conversely, lower Da values ($Da = 0.01, 0.001$) indicate less permeability, restrict fluid movement, and reduce HT efficiency, highlighting the critical role of porous medium permeability in HT dynamics. Furthermore, increasing the Re number ($Re = 500$, 1000) leads to a higher Nu number, indicating that more vital convective forces result in better HT. At lower Re numbers, natural convection plays a more significant role, while at higher Re, forced convection dominates, further enhancing HT.

4.5. Enhancement variation of Nu_{avg}

Increasing the efficiency of HT is usually accomplished by improving the performance of heat exchangers. This is obtainable by either increasing the HT power of a given device or reducing the pressure losses generated by the device. Enhancing the HT rate contributes to improved overall system performance, resulting in more efficient energy utilization and potentially significant environmental advantages. In the analysis presented in Fig. 8, investigates the impact of varying nanoparticle volume fractions ($\phi = 0\%$ to 4%), Re numbers ($Re = 300, 500, 800$, and 1000), and Da numbers ($Da = 0.1, 0.01, 0.001$) on the Nu_{avg} number enhancement $E(\%)$ at a constant Ra number ($Ra = 10^6$). This study highlights the changes in Nu_{avg}, which signifies convective HT, with respect to different volume fractions (ϕ) and permeability (Da) as well as porosity ($\epsilon = 0.4$ and 0.9) of the porous medium. In scenario (a), increasing the Re number leads to enhanced Nu_{avg} due to intensified fluid motion, promoting more efficient convective HT. Furthermore, raising ϕ further amplifies HT, especially at higher Re, as nanoparticles enhance the thermal conductivity of the fluid. However, lower Da values, indicating reduced permeability, diminish the improvement in Nu_{avg} due to restricted fluid flow, hindering effective HT. In scenario (b), increas-

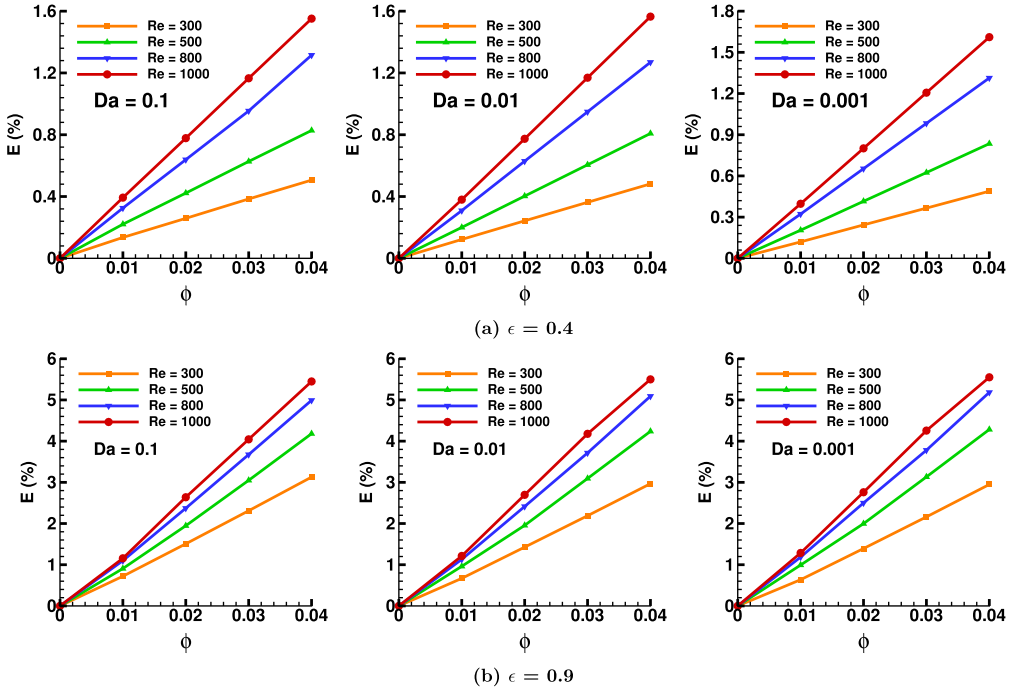

Fig. 8. Enhancement variation of Nu_{avg} for different ϕ and different Da numbers ($Da = 0.1$, 0.01, and 0.001) when $Re = 300$, 500, 800, and 1000 while $Ra = 10^6$ and $\epsilon = 0.4$ and 0.9.

ing ϕ enhances HT primarily due to the increased thermal conductivity contributed by nanoparticles, which is reflected in higher Nu_{avg} values. As the Re number increases, convective HT becomes more dominant, enhancing HT. The increased inertia of the fluid improves flow mixing and heat diffusion. Conversely, a lower Da number ($Da = 0.001$) restricts fluid flow due to the porous medium's resistance, reducing the enhancement effect. A higher Da number ($Da = 0.1$) allows smoother flow, facilitating more effective HT, particularly at elevated Re.

4.6. Results from EGEN

The concept of entropy generation (EGEN) in thermodynamics quantifies the degree of irreversibility and inefficiency inherent in actual processes. In any energy conversion or transfer, some energy is inevitably lost, leading to an increased entropy, which signifies the system's disorder. In the context of HT, this energy loss results in heat dissipation, contributing to overall entropy generation. This section analyzes EGEN in a BFS flow, exploring the effects of various parameters (Da, Ra, ϕ, ϵ). Fig. 9 shows EGEN for varying nanoparticle volume fractions (ϕ), Darcy number (Da), and a different Rayleigh numbers ($Ra = 10^5$, and 10^6) with a fixed Reynolds number ($Re = 1000$) and porosity ($\epsilon = 0.4$ and 0.9). The EGEN due to fluid friction (FF) is exceptionally high near the bottom walls of the enclosure, as the nano-coolant interacts with the heated surface during its motion. As the flow regime changes to forced convection, both components of EGEN, owing to FF (S_{ff}) and thermal effects (S_{HT}), extend from the active walls toward the core of the enclosure, indicating a more widespread irreversibility in the system. The results highlight how permeability in porous media impacts heat and flow irreversibility. Entropy generation due to viscous resistance increases with lowering Da for low permeability. At lower Da, which indicates low permeability, viscous forces dominate the flow, resulting in increased entropy generation. However, at higher Da values, where the fluid medium becomes more permeable within the porous structure, buoyancy forces drive faster, more complex fluid movement, leading to lower entropy generation. In case (a), entropy generation consistently rises as Da decreases, reflecting the greater flow complexity in a more porous medium. Increasing ϕ from 0% to 4% enhances the thermal conductivity due to nanoparticle presence and increases viscosity. This leads to more viscous dissipation and higher entropy generation, driven by steeper temperature gradients. A similar pattern emerges in cases (b) and (c). As Ra increases, the buoyancy force gets more assertive, and higher permeability leads to higher fluid velocities, lowering the viscous resistance and the entropy generation. The effect of ϕ is also apparent, with a steady rise in entropy generation as nanoparticle concentration increases, amplifying thermal conductivity and dissipation.

Fig. 10 demonstrates the EGEN in the bottom wall due to HT for different ϕ, Darcy numbers (Da), and Ra for a constant Reynolds ($Re = 1000$) number and two porosities, $\epsilon = 0.4$ and 0.9. In case (a), the entropy generation due to HT peaks within the recirculation region right after the step wall (i.e., $x/h \approx 1.4h$). As the flow progresses downstream, S_{HT} decreases significantly. Lower Da values ($Da = 0.001$) result in higher entropy generation but closer to the step wall due to the increased resistance in the porous medium for lower permeability. However, further downstream, the influence of ϕ and Da diminishes as the flow becomes fully developed. In case (b), the peak position in S_{HT} has been seen similar to case (a) but lower in magnitude, reflecting the impact of enhanced forced convection on HT irreversibility. Downstream, entropy generation decreases but remains higher than in case (a). The effects of nanoparticle volume fraction are more noticeable, with higher ϕ values leading to increased entropy generation. Lower Da values also correspond to greater thermal irreversibility, as higher flow resistance causes more significant temperature gradients in the porous medium. In case (c), the overall entropy generation is lower than in case (b) because the increased porosity reduces flow resistance. This leads to more efficient HT and lower thermal irreversibility. As in the previous cases, entropy generation is concentrated near the upstream region and decreases as the flow progresses downstream. The differences between various ϕ and Da values are less pronounced in this case due to the higher porosity, which allows for more effortless fluid movement and reduces the sensitivity of S_{HT} to these parameters.

4.7. Performance evaluation criteria (PEC)

In the illustration provided in Fig. 11, the impact of buoyancy-driven flow on the Performance Evaluation Criteria (PEC) for porous media is demonstrated. The analysis considers various porosity values

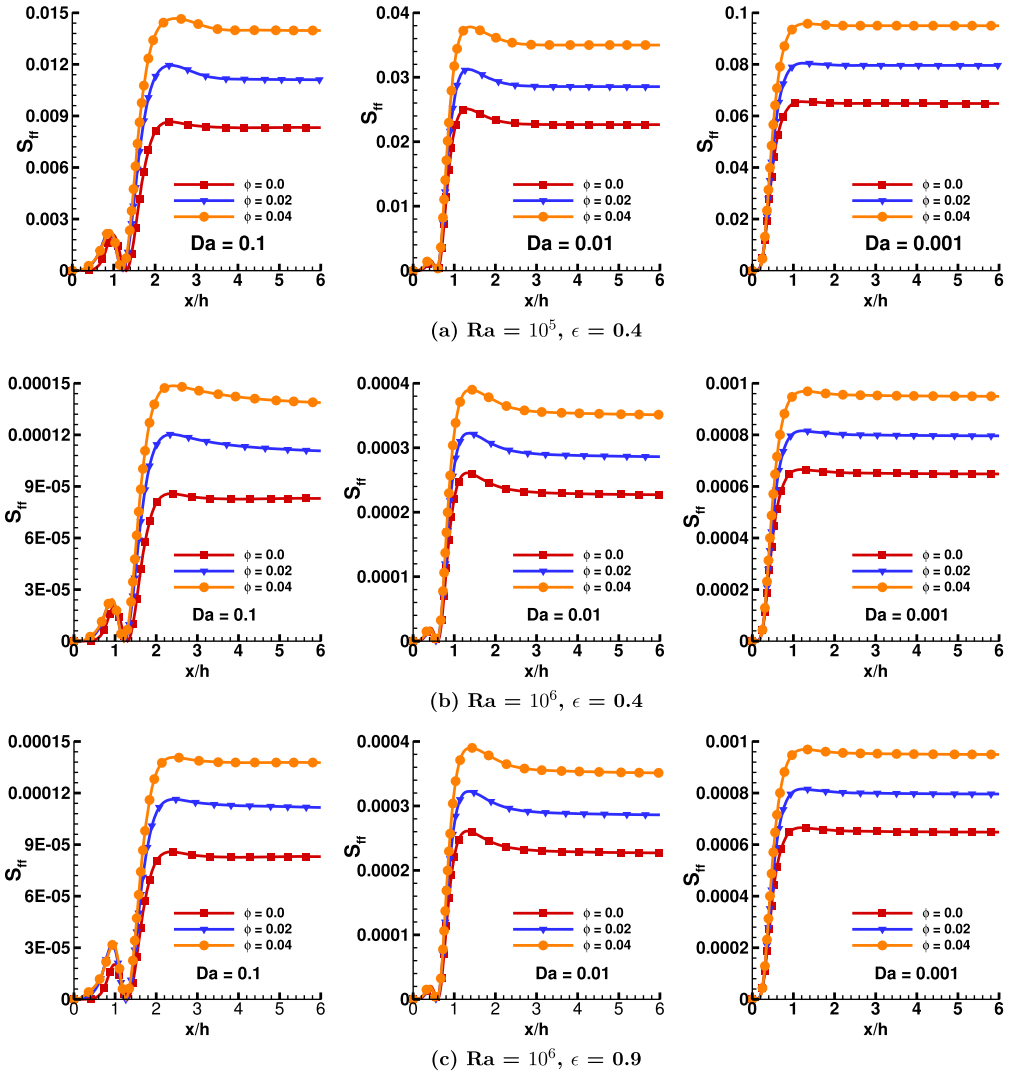

Fig. 9. Entropy generation due to FF on the heated downstream wall for different ϕ, Da, and Ra numbers, constant $Re = 1000$ numbers, and $\epsilon = 0.4$ and 0.9.

$\epsilon = 0.4, 0.9$, and $Da = 0.1$, 0.01, and 0.001 across a range of Reynolds (Re) and Rayleigh (Ra) numbers. This examination emphasizes how the interaction between flow strength, buoyancy forces, porous medium resistance, and non-Newtonian fluid behavior affects HT performances. Across all cases, PEC decreases as ϕ increases from 0% to 4%. This reduction is primarily attributed to the escalation in viscosity resulting from higher ϕ, which counteracts the improved thermal conductivity of the nanofluid. For non-Newtonian fluids with respect to ϕ, heightened non-Newtonian viscosity leads to increased resistance to flow, increasing the nanoparticle weight percentage, causing energy dissipation, and reducing HT efficiency. In scenario (a), the flow experiences higher resistance from the porous medium due to low porosity ($\epsilon = 0.4$), resulting in lower PEC values compared to the high porous medium structure ($\epsilon = 0.9$). Despite the decline in PEC as ϕ increases, the performance of convective HT is more prominent, especially at higher Ra numbers. Elevated Re numbers further enhance convective HT, helping alleviate the reduction in PEC caused by the increase in viscosity. In scenario (b), the buoyancy force gets stronger within the low porous medium structure. The PEC shows a decreasing trend as ϕ increases, indicating a more significant impact of viscosity on the HT performance. Buoyancy-driven convection takes precedence, and although higher Ra numbers partially offset the performance loss, the overall PEC still diminishes due to increased viscous resistance and pressure drop. In scenario (c), the porosity of the medium gets stronger with different permeability conditions of the flow. As ϕ increases, there is a marked decline in PEC, reflecting the substantial impact of flow resistance and viscous dissipation. Even with higher Ra numbers, the constrained flow and reduced thermal diffusion result in a notable drop in the HT efficiency.

4.8. Engineering relevance of parametric findings

This study investigates non-Newtonian nanofluid flow through a porous channel, focusing on the effects of Re number, Da number, Ra number, ϵ, and ϕ on streamlines, isotherms, HT, and flow behavior. The analysis captures how these parameters influence recirculation zones, wall shear stress, entropy generation, and overall thermal performance.

- Section 4.1: Lower Da numbers reduce permeability and transition the system from convection-dominated to conduction-dominated regimes, which is critical for designing thermal insulators and porous heat exchangers in compact energy systems.
- Section 4.2: Increasing ϕ and decreasing Da result in higher wall shear stress, offering insight into balancing flow resistance and thermal efficiency in microchannel cooling systems and fibrous porous media.
- Section 4.3: Recirculation length decreases with higher ϕ and lower Da, while increasing Re elongates it. These trends inform the optimization of reattachment flow zones for enhanced mixing and cooling in MEMS and compact thermal devices.

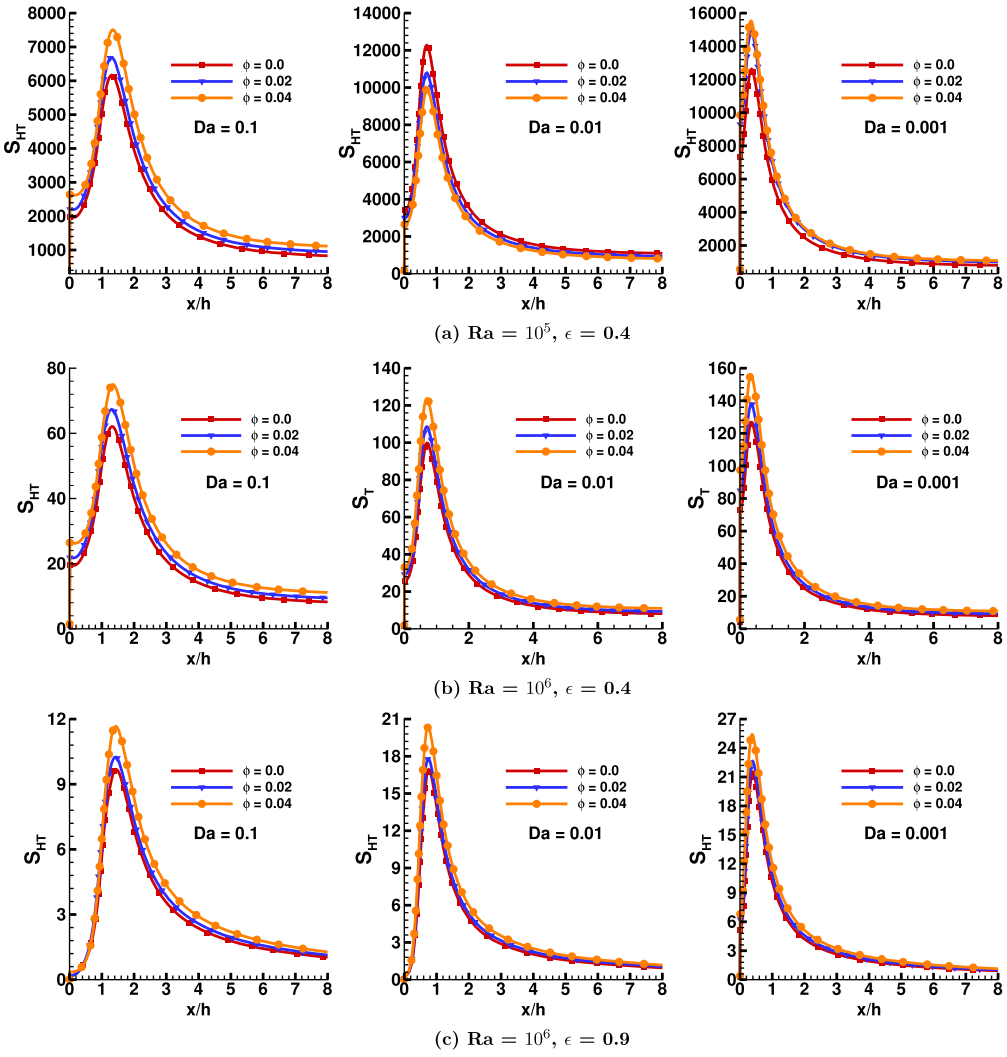

(a) Ra $= 10^5$, $\epsilon = 0.4$

(b) Ra $= 10^6$, $\epsilon = 0.4$

(c) Ra $= 10^6$, $\epsilon = 0.9$

Fig. 10. Entropy generation due to heat transfer on the heated downstream wall for different ϕ, Da, and Ra numbers, constant $Re = 1000$ numbers, and $\epsilon = 0.4$ and 0.9.

- Section 4.4: Higher Re and lower ϕ significantly increase the Nu_{avg} number, supporting the design of energy-efficient cooling technologies, such as battery thermal management and power electronics.
- Section 4.5: The percentage HT enhancement peaks at lower ϕ and higher Re, emphasizing the practical value of using low-concentration nanofluids for effective heat dissipation with minimal pumping power.
- Section 4.6: EGEN decreases with improved thermal conductivity and flow uniformity, which is essential for minimizing energy loss in industrial HT systems and porous media flow configurations.
- Section 4.7: PEC increases with Re but decreases with ϕ, highlighting a trade-off between HT and pressure loss. This metric aids engineers in selecting optimal nanoparticle concentrations for real-world thermal applications.

5. Conclusion

This research delves into the behavior of non-Newtonian Al_2O_3-water nanofluids flowing through a porous BFS channel, which has greatly enhanced our comprehension of the interplay between fluid dynamics and heat transfer within a non-Darcy porous medium. Five pivotal parameters were adjusted: the Re number, Da number, Ra number, nanoparticle volume fraction ϕ, and porosity ϵ. Altering the Re numbers proved especially impactful, significantly influencing flow behavior and the emergence of recirculation areas. The key insights from this analysis can be encapsulated as follows:

- The addition of Al_2O_3 nanoparticles increases HT efficiency by 1.54%. However, this improvement comes with an 11.92% increase in pressure drop, significantly raising the required pumping power at $Re = 1000$, $Ra = 10^6$, $Da = 0.1$, and $\phi = 4\%$.
- Increasing the Reynolds number (Re) from 300 to 1000 increases the reattachment length by about 229% and shifts the separation point downstream. A nanoparticle volume fraction of $\phi = 4\%$ reduces the recirculation zone size by 35%, enhancing fluid mixing and heat transfer near the step.
- Reducing Da from 0.1 to 0.001 increases the skin friction coefficient (C_f) by 233.33% at $Re = 1000$, with $Ra = 10^6$ and $\phi = 4\%$. This shows greater resistance in the porous medium, particularly in the recirculation region.
- Doubling the Re number for shear-thinning (Al_2O_3) nano-coolants leads to a 50% reduction in the skin friction coefficient (C_f) at $\phi = 4\%$, underscoring the greater influence of inertial forces over viscous effects in porous media flows.
- At $\phi = 4\%$, increasing ϵ from 0.4 to 0.99 results in a significant decrease in the average Nusselt number (Nu_{avg}) by approximately 90.56%, 90.85%, and 90.74% for Darcy numbers (Da) of 0.1, 0.01, and 0.001, respectively, under $Re = 1000$ and $Ra = 10^6$ conditions.

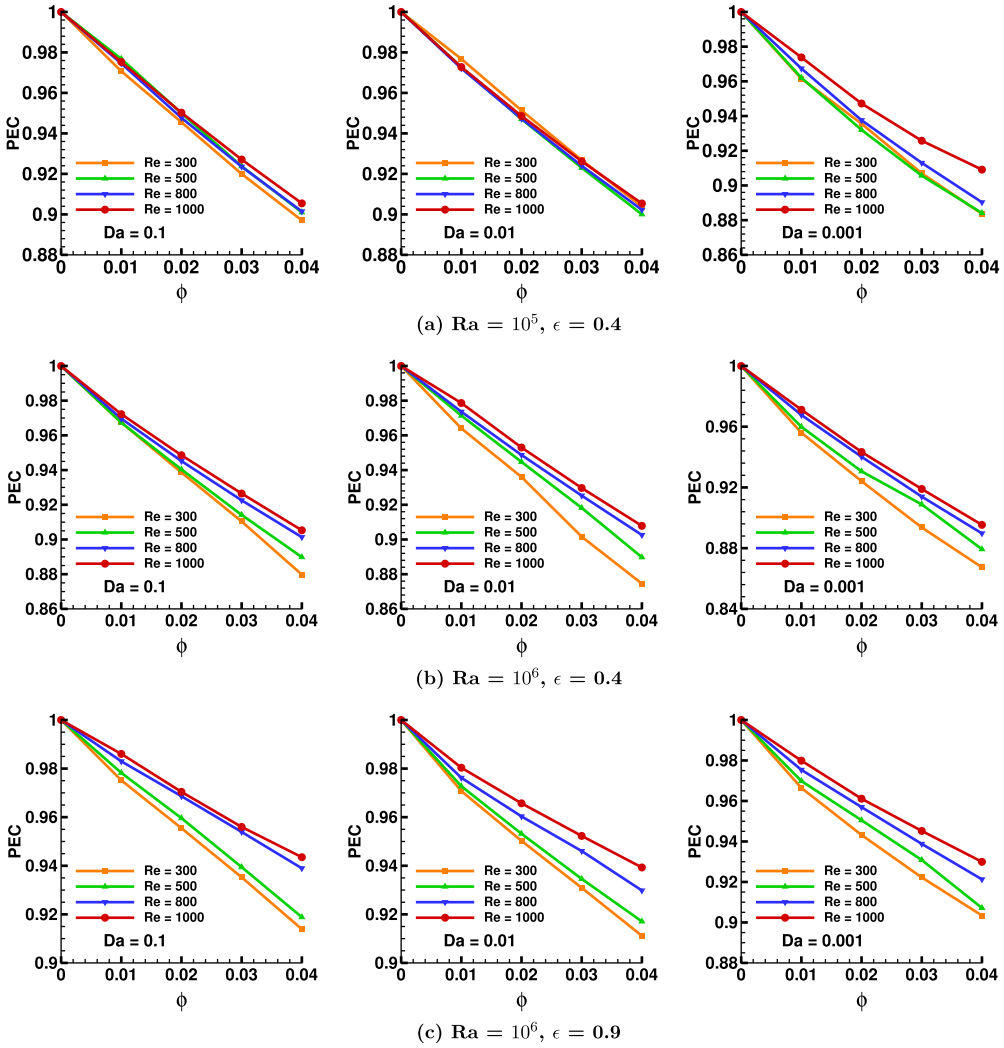

Fig. 11. Performance evaluation criterion (PEC) of non-Newtonian nanofluid for different values of ϕ, Re, Da, and Ra while $\epsilon = 0.4$ and 0.9.

- The use of shear-thinning nanofluid with $\phi = 4\%$, $Re = 1000$ at $\epsilon = 0.4$ at high $Ra = 10^6$ led to significant increases in the average Nu number by 11.60%, 11.15%, and 10.60% for $Da = 0.1$, 0.01, and 0.001, respectively.
- The entropy generation from heat transfer (S_{HT}) peaks at $x/h \approx 1.4$ for $Re = 1000$, $Ra = 10^6$, $\phi = 4\%$, and $Da = 0.1$. This shows that higher nanoparticle concentration and flow resistance increase thermal irreversibility, reducing system efficiency.
- The PEC criterion decreases with ϕ by 85% as for the extreme case of $Da = 0.001$ and $Ra = 10^6$. This suggests that while nanoparticles improve heat transfer, greater pumping power is needed for enhanced thermal performance. However, higher flow strength (greater Re) improves PEC quality.

The findings of this study provide valuable insights for the design and optimization of heat transfer (HT) systems that use non-Newtonian fluids flowing through generalized non-Darcian porous media. Future research may explore non-equilibrium thermal conditions in porous media, the effect of magnetic induction and Hall currents by examining single-phase non-homogeneous ferrofluids within the BFS domain. While this study limits the Reynolds number to a laminar flow range less than 1000, future studies could investigate higher Reynolds numbers to assess turbulence and its impact on enhancing heat transfer performance.

CRediT authorship contribution statement

Zarin Akter: Writing – original draft, Visualization, Validation, Software, Investigation, Formal analysis, Data curation. **Preetom Nag:** Writing – original draft, Supervision, Software, Project administration, Methodology, Funding acquisition, Conceptualization. **Hasina Akter:** Writing – review & editing, Formal analysis. **Md. Mamun Molla:** Writing – review & editing, Formal analysis. **Goutam Saha:** Writing – review & editing, Formal analysis.

Funding

North South University CTRG research grant (CTRG-23-SEPS-31) and the Ministry of Science and Technology (MOST) (SRG-246481), Government of the People's Republic of Bangladesh.

Declaration of competing interest

The authors declare that they have no known competing financial interests or personal relationships that could have appeared to influence the work reported in this paper.

Data availability

Data will be made available on request.

References

[1] Z. Abbas, M. Rafiq, M. Arslan, N. Rangra, Optimizing power and cooling: sor-based computational analysis of hybrid nanoliquid flow in Darcy porous medium, Results Eng. 26 (2025) 104602.

[2] P. Kameswaran, Z. Makukula, P. Sibanda, S. Motsa, P. Murthy, A new algorithm for internal heat generation in nanofluid flow due to a stretching sheet in a porous medium, Int. J. Numer. Methods Heat Fluid Flow 24 (5) (2014) 1020–1043.

[3] S. Kemparaju, H.K. Swamy, M. Sankar, F. Mebarek-Oudina, Impact of thermal and solute source-sink combination on thermosolutal convection in a partially active porous annulus, Phys. Scr. 97 (5) (2022) 055206.

[4] G. Amhalhel, P. Furmanski, Problems of modeling flow and heat transfer in porous media, J. Power Technol. 85 (1997) 55.

[5] R. Kaur, A. Chandra, S. Sharma, Momentum transfer across a semi-circular porous cylinder attached to a channel wall, Meccanica 56 (2021) 2219–2241.

[6] R. Kaur, S. Sharma, A. Chandra, Effects of viscous dissipation, temperature dependent thermal conductivity, and local thermal non-equilibrium on the heat transfer in a porous channel to Casson fluid, Can. J. Chem. Eng. 102 (11) (2024) 3744–3755.

[7] G. Bourantas, E. Skouras, V. Loukopoulos, V. Burganos, Heat transfer and natural convection of nanofluids in porous media, Eur. J. Mech. B, Fluids 43 (2014) 45–56.

[8] S.U. Choi, J.A. Eastman, Enhancing thermal conductivity of fluids with nanoparticles, Tech. Rep., Argonne National Lab. (ANL), Argonne, IL, United States, 1995.

[9] S. Ganguly, S. Sikdar, S. Basu, Experimental investigation of the effective electrical conductivity of aluminum oxide nanofluids, Powder Technol. 196 (3) (2009) 326–330.

[10] K. Swain, S. Mishra, Flow and heat transfer analysis of water-based copper nanofluid over a nonlinearly stretching sheet: a numerical approach, Int. J. Ambient Energy 43 (1) (2022) 5810–5824.

[11] S. Mishra, K. Swain, R. Dalai, Joule heating and viscous dissipation effects on heat transfer of hybrid nanofluids with thermal slip, Iran. J. Sci. Technol. Trans. Mech. Eng. 48 (2) (2024) 531–539.

[12] N. Keerthi Reddy, M. Sankar, Buoyant convective transport of nanofluids in a non-uniformly heated annulus, J. Phys. Conf. Ser. 1597 (1) (2020) 012055.

[13] E. Abu-Nada, Application of nanofluids for heat transfer enhancement of separated flows encountered in a backward facing step, Int. J. Heat Fluid Flow 29 (1) (2008) 242–249.

[14] I. Pop, T. Groșan, C. Revnic, A.V. Roșca, Unsteady flow and heat transfer of nanofluids, hybrid nanofluids, micropolar fluids and porous media: a review, Therm. Sci. Eng. Prog. 46 (2023) 102248.

[15] J. Li, H. Zhai, L. Shi, N. Tan, Y. Zhang, C. Huang, Experimental analysis of convective boiling heat transfer and nanoparticle deposition effect of tio2-h2o nanofluids in microchannels, Therm. Sci. Eng. Prog. 47 (2024) 102282.

[16] A. Shenoy, Non-Newtonian fluid heat transfer in porous media 24 (1994) 101–190.

[17] L. Yang, K. Du, A comprehensive review on the natural, forced, and mixed convection of non-Newtonian fluids (nanofluids) inside different cavities, J. Therm. Anal. Calorim. 140 (2020) 2033–2054.

[18] I. Abbas, S. Hasnain, M. Saqib, D.S. Mashat, Computational study on the influence of non-Newtonian nano fluids in fluid flow and heat transfer over a permeable surface with injection and suction, Sci. Iran. (2023).

[19] J.P. Denier, R.E. Hewitt, Asymptotic matching constraints for a boundary-layer flow of a power-law fluid, J. Fluid Mech. 518 (2004) 261–279.

[20] A. Singh, N. Kishore, Mixed convection of shear-thinning nanofluids past unconfined elliptical cylinders in vertical upward flow, Int. J. Therm. Sci. (2017).

[21] H. Chen, Y. Ding, A. Lapkin, X. Fan, Rheological behavior of ethylene glycol titanate nanotube nanofluids, J. Nanopart. Res. (2009).

[22] M. Hojjat, S.G. Etemad, R. Bagheri, J. Thibault, Rheological characteristics of non-Newtonian nanofluids: experimental investigation, Int. Commun. Heat Mass Transf. 38 (2) (2011) 144–148.

[23] F. Salehi, M. Inanloodoghouz, M. Karami, Rheological properties of carboxymethyl cellulose (cmc) solution: impact of high intensity ultrasound, Ultrason. Sonochem. 101 (2023) 106655.

[24] A. Benchabane, K. Bekkour, Rheological properties of carboxymethyl cellulose (cmc) solutions, Colloid Polym. Sci. 286 (10) (2008) 1173–1180.

[25] A.K. Santra, S. Sen, N. Chakraborty, Study of heat transfer augmentation in a differentially heated square cavity using copper–water nanofluid, Int. J. Therm. Sci. 47 (9) (2008) 1113–1122.

[26] S. Nazari, R. Ellahi, M. Sarafraz, M.R. Safaei, A. Asgari, O.A. Akbari, Numerical study on mixed convection of a non-Newtonian nanofluid with porous media in a two lid-driven square cavity, J. Therm. Anal. Calorim. 140 (2020) 1121–1145.

[27] P. Zainith, N.K. Mishra, Experimental investigations on stability and viscosity of carboxymethyl cellulose (cmc)-based non-Newtonian nanofluids with different nanoparticles with the combination of distilled water, Int. J. Thermophys. 42 (10) (2021) 137.

[28] Z.H. Khan, W.A. Khan, S.M. Ibrahim, K. Swain, Z. Huang, Impact of multiple slips and thermal radiation on heat and mass transfer in mhd Maxwell hybrid nanofluid flow over porous stretching sheet, Case Stud. Therm. Eng. 61 (2024) 104906.

[29] H. Ameur, Y. Menni, Non-Newtonian fluid flows through backward-facing steps, SN Appl. Sci. 1 (12) (2019) 1717.

[30] G. Ilio, D. Chiappini, G. Bella, A comparison of numerical methods for non-Newtonian fluid flow in a sudden expansion, Int. J. Mod. Phys. C (2016).

[31] A. Mokhefi, E.R. di Schio, P. Valdiserri, C. Biserni, D. Derbal, Numerical Study of the Thermo-Hydrodynamic Behavior of a Non-newtonian Nanofluid in a Backward Facing Step, Journal of Physics: Conference Series, vol. 2685, IOP Publishing, 2024, p. 012074.

[32] L. Chen, K. Asai, T. Nonomura, G. Xi, T. Liu, A review of backward-facing step (bfs) flow mechanisms, heat transfer and control, Therm. Sci. Eng. Prog. 6 (2018) 194–216.

[33] A. Al-Aswadi, H. Mohammed, N. Shuaib, A. Campo, Laminar forced convection flow over a backward facing step using nanofluids, Int. Commun. Heat Mass Transf. 37 (8) (2010) 950–957.

[34] K. Khanafer, B. Al-Azmi, A. Al-Shammari, I. Pop, Mixed convection analysis of laminar pulsating flow and heat transfer over a backward-facing step, Int. J. Heat Mass Transf. 51 (25–26) (2008) 5785–5793.

[35] B.F. Armaly, F. Durst, J. Pereira, B. Schönung, Experimental and theoretical investigation of backward-facing step flow, J. Fluid Mech. 127 (1983) 473–496.

[36] T. Lee, D. Mateescu, Experimental and numerical investigation of 2-d backward-facing step flow, J. Fluids Struct. 12 (6) (1998) 703–716.

[37] E. Erturk, Numerical solutions of 2-d steady incompressible flow over a backward-facing step, part I: high Reynolds number solutions, Comput. Fluids 37 (6) (2008) 633–655.

[38] K. Swain, S.M. Ibrahim, G. Dharmaiah, S. Noeiaghdam, Numerical study of nanoparticles aggregation on radiative 3d flow of Maxwell fluid over a permeable stretching surface with thermal radiation and heat source/sink, Results Eng. 19 (2023) 101208.

[39] W. Wang, X. Xu, Z. Li, Three-dimensional numerical analysis of turbulent heat transfer in backward-facing step flow with porous medium, Int. J. Heat Mass Transf. 179 (2023) 121723.

[40] M.T. Al-Asadi, H.A. Mohammed, M.C. Wilson, Heat transfer characteristics of conventional fluids and nanofluids in micro-channels with vortex generators: a review, Energies 15 (3) (2022) 1245.

[41] M. Mansour, S. Siddiqa, R.S.R. Gorla, A. Rashad, Effects of heat source and sink on entropy generation and mhd natural convection of al2o3-cu/water hybrid nanofluid filled with square porous cavity, Therm. Sci. Eng. Prog. 6 (2018) 57–71.

[42] S. Nandapurkar, A. Jani, Entropy generation in turbulent flow over a backward-facing step filled with porous medium, in: Proceedings of the ASME 2023 17th International Conference on Nanochannels, Microchannels, and Minichannels, American Society of Mechanical Engineers, 2023.

[43] K. Amit, A. Datta, N. Biswas, S. Das, P. Das, Designing of microsink to maximize the thermal performance and minimize the entropy generation with the role of flow structures, Int. J. Heat Mass Transf. 176 (2021) 121421.

[44] M. Kong, S. Lee, Performance evaluation of al2o3 nanofluid as an enhanced heat transfer fluid, Adv. Mech. Eng. 12 (8) (2020) 1687814020952277.

[45] M. Irandoost Shahrestani, A. Maleki, M. Safdari Shadloo, I. Tlili, Numerical investigation of forced convective heat transfer and performance evaluation criterion of al2o3/water nanofluid flow inside an axisymmetric microchannel, Symmetry 12 (1) (2020) 120.

[46] R. Kaur, S. Sharma, A. Chandra, Forced convection heat transfer from confined circular/semi-circular heaters and coolers with various orientations, Can. J. Chem. Eng. 102 (11) (2024) 3756–3775.

[47] T. Mahmud, T. Chowdhury, P. Nag, M.M. Molla, Entropy production associated with magnetohydrodynamics (mhd) thermo-solutal natural convection of non-Newtonian mwcnt-sio2-eg hybrid nano-coolant, Heliyon 10 (15) (2024).

[48] M. Zawrah, R. Khattab, L. Girgis, H.E. Daidamony, R.E. Abdel Aziz, Stability and electrical conductivity of water-base al2o3 nanofluids for different applications, HBRC J. 12 (3) (2016) 227–234.

[49] A.A. Minea, A review on electrical conductivity of nanoparticle-enhanced fluids, Nanomaterials 9 (11) (2019).

[50] P. Nithiarasu, K. Seetharamu, T. Sundararajan, Natural convective heat transfer in a fluid saturated variable porosity medium, Int. J. Heat Mass Transf. 40 (16) (1997) 3955–3967.

[51] M. Tasmin, P. Nag, Z.T. Hoque, M.M. Molla, Non-Newtonian effect on heat transfer and entropy generation of natural convection nanofluid flow inside a vertical wavy porous cavity, SN Appl. Sci. 3 (2021) 1–29.

[52] H.C. Brinkman, A calculation of the viscous force exerted by a flowing fluid on a dense swarm of particles, Flow Turbul. Combust. 1 (1) (1949) 27–34.

[53] V.D. Ingenieure, Zeitschrift der Vereines Deutscher Ingenieure, vol. 53, Rudolph Gaertner, 1909.

[54] H.K. Swamy, M. Sankar, N.K. Reddy, M.A. Manthari, Double diffusive convective transport and entropy generation in an annular space filled with alumina-water nanoliquid, Eur. Phys. J. Spec. Top. 231 (13) (2022) 2781–2800.

[55] C.-C. Liao, W.-K. Li, H.-E. Lin, Heat transfer enhancement in microchannel systems through geometric modification of vortex generators and nanofluid integration: a numerical study, Results Eng. (2025) 104138.

[56] H.E. Patel, K. Anoop, T. Sundararajan, S.K. Das, A micro-convection model for thermal conductivity of nanofluids, in: International Heat Transfer Conference 13, Begel House Inc., 2006.

[57] T. Mahmud, P. Nag, M.M. Molla, S.C. Saha, Convective heat transfer efficacy of an experimentally observed non-Newtonian mwcnt-fe3o4-eg hybrid nanofluid in a driven enclosure with a heated cylinder, Int. J. Therm. Sci. 204 (2024) 109203.

[58] A.M. Hassan, M.A. Alomari, A. Alajmi, A.M. Sadeq, F. Alqurashi, M.A. Flayyih, Numerical analysis of nano-encapsulated pcm magnetohydrodynamics double-diffusive

convection and entropy generation in vertical enclosures with porous layer, Results Eng. 24 (2024) 103579.
[59] G. Lauriat, V. Prasad, Non-Darcian effects on natural convection in a vertical porous enclosure, Int. J. Heat Mass Transf. 32 (11) (1989) 2135–2148.
[60] H. Herwig, The role of entropy generation in momentum and heat transfer, J. Heat Transf. (2012).
[61] M. Esmaeilpour, M. Abdollahzadeh, Free convection and entropy generation of nanofluid inside an enclosure with different patterns of vertical wavy walls, Int. J. Therm. Sci. 52 (2012) 127–136.
[62] A. Mchirgui, N. Hidouri, M. Magherbi, A.B. Brahim, Entropy generation in double-diffusive convection in a square porous cavity using Darcy–Brinkman formulation, Transp. Porous Media 93 (2012) 223–240.
[63] G.G. Ilis, M. Mobedi, B. Sunden, Effect of aspect ratio on entropy generation in a rectangular cavity with differentially heated vertical walls, Int. Commun. Heat Mass Transf. 35 (6) (2008) 696–703.
[64] J. Mewis, N.J. Wagner, Colloidal Suspension Rheology, vol. 10, Cambridge University Press, Cambridge, 2012.
[65] P. Nag, M.M. Molla, Double-diffusive natural convection of non-Newtonian nanofluid considering thermal dispersion of nanoparticles in a vertical wavy enclosure, AIP Adv. 11 (9) (2021).
[66] M.M. Molla, P. Nag, S. Thohura, A. Khan, A graphics process unit-based multiple-relaxation-time lattice Boltzmann simulation of non-Newtonian fluid flows in a backward-facing step, Computation 8 (3) (2020) 83.